



1 Centrifugal and symmetric instability during Ekman adjustment of the

2 bottom boundary layer

3 Jacob O. Wenegrat*

4 Department of Atmospheric and Oceanic Science, University of Maryland, College Park

5 Leif N. Thomas

6 Earth System Science, Stanford University

7 *Corresponding author address: Dept. of Atmospheric and Oceanic Sciences, University of Mary-
8 land, 4254 Stadium Dr., College Park, MD, 20742.
9 E-mail: wenegrat@umd.edu

ABSTRACT

10 Flow along isobaths of a sloping lower boundary generates an across-isobath
11 Ekman transport in the bottom boundary layer. When this Ekman transport is
12 down the slope it causes convective mixing — much like a downfront wind in
13 the surface boundary layer — destroying stratification and potential vorticity.
14 In this manuscript we show how this can lead to the development of a forced
15 centrifugal or symmetric instability regime, where the potential vorticity flux
16 generated by friction along the boundary is balanced by submesoscale insta-
17 bilities that return the boundary layer potential vorticity to zero. This balance
18 provides a strong constraint on the boundary layer evolution, which we use
19 to develop theory that explains the evolution of the boundary layer thickness,
20 the rate at which the instabilities extract energy from the geostrophic flow
21 field, and the magnitude and vertical structure of the dissipation. Finally, we
22 show using theory and a high-resolution numerical model how the presence of
23 centrifugal or symmetric instabilities alters the time-dependent Ekman adjust-
24 ment of the boundary layer, delaying Ekman buoyancy arrest and enhancing
25 the total energy removed from the balanced flow field. Submesoscale insta-
26 bilities of the bottom boundary layer may therefore play an important, largely
27 overlooked, role in the energetics of flow over topography in the ocean.

28 **1. Introduction**

29 The ocean bottom boundary layer (BBL) over sloping topography often has a structure reminis-
30 cent of a surface mixed layer front, with isopycnals that slope downward from the interior towards
31 the topography (figure 1). One way that this frontal BBL structure can develop is when interior
32 flow along isobaths of a sloping lower boundary forces an across-isobath bottom Ekman transport
33 (MacCready and Rhines 1991). This Ekman transport follows the sloping lower boundary, which
34 crosses isopycnals whenever the interior is stratified, thereby generating an advective flux of buoy-
35 ancy. When the transport is towards deeper water (downslope), the advective buoyancy flux brings
36 buoyant water down along the bottom, leading to convective mixing, which on the slope acts to
37 increase the horizontal buoyancy gradient while reducing the vertical gradient.

38 The case of downslope Ekman transport is therefore closely analogous to the case of a downfront
39 wind stress (Thomas 2005; Thomas and Ferrari 2008), where a wind aligned with a frontal jet
40 drives an Ekman transport that is directed from the dense side to the light side of a surface ocean
41 front. This Ekman buoyancy flux has been shown to modify the surface boundary layer in a wide
42 variety of ways, one of the most consequential of which is through the generation of symmetric
43 instability (SI), a fast growing submesoscale instability associated with 2D overturning circulations
44 in the cross-front plane (Stone 1966; Haine and Marshall 1998). A partial list of the aspects of the
45 surface boundary layer evolution which SI is known to affect includes the rates of: mixed-layer
46 deepening, entrainment, restratification, kinetic energy dissipation, and buoyancy mixing (Taylor
47 and Ferrari 2010; D'Asaro et al. 2011; Thomas et al. 2013, 2016).

48 Several lines of evidence point to the existence of similar processes in the BBL, starting with
49 theoretical and modeling work by Allen and Newberger (1998), who noted that when the BBL
50 is in thermal wind balance (the ‘arrested’ Ekman layer, Garrett et al. 1993) it can be unstable to

51 growing symmetric modes, suggesting the incompleteness of 1D theory. Using 2D simulations
52 they investigated the finite-amplitude behavior of SI, arguing that instabilities are likely found
53 both in response to Ekman adjustment of the boundary layer to an interior flow and in response
54 to downwelling favorable surface winds (Allen and Newberger 1993, 1998). More recent ideal-
55 ized 3D numerical simulations of a tidal mixing front (Brink and Cherian 2013), and dense shelf
56 overflows (Yankovsky and Legg 2019), likewise indicate the presence of both SI and baroclinic
57 modes, consistent with the predictions of Wenegrat et al. (2018). Finally, perhaps the most com-
58 pelling evidence currently available comes from recent observations taken in the Southern Ocean,
59 which showed that downslope Ekman flows in the deep ocean, generated by the Antarctic bottom
60 water flowing along steep topography, led to conditions conducive to symmetric and centrifugal
61 instabilities (CI, Naveira Garabato et al. 2019). These conditions were also associated with en-
62 hanced turbulent dissipation rates (Naveira Garabato et al. 2019), similar to observations of SI in
63 the surface boundary layer (D'Asaro et al. 2011).

64 The primary goal of this paper is therefore to examine centrifugal and symmetric instability
65 in the BBL in the case where a steady interior flow over uniformly sloping topography drives a
66 downslope Ekman transport. We focus on the time-dependent adjustment process, and the devel-
67 opment of a ‘forced’ regime where downslope Ekman buoyancy fluxes maintain persistent SI/CI.
68 The similarity between downslope and across-front wind-driven Ekman transports is used to adapt
69 the insightful derivations provided in Taylor and Ferrari (2010, hereinafter TF10) for the surface
70 boundary layer to the case of a BBL over sloping topography. This allows us to extend earlier work
71 on this topic to provide a theoretical framework that explains many aspects of the BBL evolution
72 in the presence of SI and CI, including how the boundary layer height and stratification evolve, the
73 rate at which the instabilities extract energy from the mean flow, and the magnitude and vertical
74 structure of the turbulent dissipation.

75 The manuscript is organized as follows. In section 2 we introduce the high-resolution numerical
76 model we use to test the theory, and provide a brief qualitative discussion of the evolution of two
77 representative simulations. In section 3 we develop the theory of the BBL evolution in the presence
78 of SI/CI, and test the predictions against the numerical simulations. In section 4 we show how
79 SI/CI modifies the energetics of the BBL and provide simple scalings for the turbulent dissipation
80 that reproduce the numerical results. Finally, in section 5 we discuss how SI/CI modifies the
81 classical 1D conception of the Ekman adjustment of the BBL.

82 **2. Numerical Simulations**

83 *a. Numerical model configuration*

84 To explore the role of instabilities during Ekman adjustment of the BBL we perform high-
85 resolution numerical simulations of a stratified flow oriented along isobaths of a sloping bottom.
86 The domain setup is idealized, assuming uniform topographic slope (θ), periodicity in the along-
87 and across isobath directions, a steady barotropic interior flow (V_∞), and uniform interior stratifi-
88 cation (N_∞^2 , figure 1). Our interest is in the SI/CI modes, hence we only consider the case where
89 the interior flow generates downwelling in the bottom Ekman layer (ie. $V_\infty > 0$ in the Northern
90 Hemisphere for the geometry shown in figure 1).

91 It is useful to work in a coordinate system rotated to align with the sloping bottom (figure 1),
92 where x is the across-isobath (across-slope) direction, y is the along-isobath (along-slope) di-
93 rection, and z is the slope-normal direction (defined such that the bottom is at $z = 0$). When
94 coordinates or variables are referenced in the standard, non-rotated, coordinate system they
95 will be indicated using hat notation (ie. \hat{z} is parallel to the direction of gravitational acceler-
96 ation). Separating the total velocity and buoyancy fields into interior (denoted with subscript

⁹⁷ ∞) and perturbation quantities (denoted by lowercase variables), such that $\mathbf{u}_T = (u, v + V_\infty, w)$
⁹⁸ and $b_T = b + N_\infty^2(z \cos \theta + x \sin \theta)$, the equations governing the perturbations are (Wenegrat et al.
⁹⁹ 2018),

$$\frac{\partial u}{\partial t} + \mathbf{u}_T \cdot \nabla u - f \cos \theta v = -\frac{1}{\rho_o} \frac{\partial p}{\partial x} + b \sin \theta + v \nabla^2 u, \quad (1)$$

$$\frac{\partial v}{\partial t} + \mathbf{u}_T \cdot \nabla v - f \sin \theta w + f \cos \theta u = -\frac{1}{\rho_o} \frac{\partial p}{\partial y} + v \nabla^2 v, \quad (2)$$

$$\frac{\partial w}{\partial t} + \mathbf{u}_T \cdot \nabla w + f \sin \theta v = -\frac{1}{\rho_o} \frac{\partial p}{\partial z} + b \cos \theta + v \nabla^2 w, \quad (3)$$

$$\frac{\partial b}{\partial t} + \mathbf{u}_T \cdot \nabla b + u N_\infty^2 \sin \theta + w N_\infty^2 \cos \theta = \kappa \nabla^2 b, \quad (4)$$

$$\nabla \cdot \mathbf{u} = 0. \quad (5)$$

¹⁰⁰ Note that the use of periodic boundary conditions in the across-slope (x) direction requires that the
¹⁰¹ mean across-slope buoyancy gradient remains fixed in time, with magnitude $N_\infty^2 \sin \theta$. This setup
¹⁰² is therefore similar to the ‘frontal-zone’ configuration commonly used in spectral simulations of
¹⁰³ surface boundary layer fronts, where a fixed magnitude horizontal buoyancy gradient is imposed
¹⁰⁴ (eg. TF10; Thomas and Taylor 2010). Importantly however, in the BBL case both the mean
¹⁰⁵ horizontal buoyancy gradient, and the mean vertical vorticity, are free to evolve in time.

¹⁰⁶ Bottom boundary conditions are given by,

$$u = 0, \quad v + V_\infty = 0, \quad w = 0, \quad \frac{\partial b}{\partial z} + N_\infty^2 \cos \theta = 0, \quad \text{at } z = 0. \quad (6)$$

¹⁰⁷ These equations are solved numerically using the spectral code Dedalus (Burns et al. 2019) in a
¹⁰⁸ 2D domain ($x - z$) that is periodic in the across and along-isobath directions (x and y), and bounded
¹⁰⁹ by rigid walls in the slope-normal direction (z). The 2D domain allows for computationally ef-
¹¹⁰ ficient exploration of the 2D SI/CI overturning instabilities, but will suppress the emergence of
¹¹¹ 3D baroclinic modes expected after a transient SI phase in cases with low interior slope Burger
¹¹² number, $S_\infty = N_\infty \theta / f$ (Brink and Cherian 2013; Wenegrat et al. 2018). In regions with large slope

¹¹³ Burger number topographic suppression of the baroclinic growth rates allows for persistent SI/CI
¹¹⁴ even in 3D simulations (Wenegrat et al. 2018).

¹¹⁵ In all simulations the effective resolution after de-aliasing is $\Delta x = 1$ m and $\Delta z = 0.01 - 1.2$ m,
¹¹⁶ with enhanced resolution near the lower and upper-boundaries. The domain size is 1 km in the
¹¹⁷ across-slope (x) direction and 200 m in the slope-normal (z) direction, except where larger domains
¹¹⁸ were determined to be necessary to fully resolve the instabilities and boundary layer evolution
¹¹⁹ (as indicated in table 1). A sponge region with Rayleigh damping of perturbations is applied in
¹²⁰ the upper 20 m of the domain to reduce wave reflection (as in TF10). A constant viscosity and
¹²¹ diffusivity of $\nu = \kappa = 10^{-4}$ m² s⁻¹ are used, again consistent with TF10, giving a laminar Ekman
¹²² layer depth of $\delta_e = \sqrt{2\nu/f} = 1.4$ m. The near-wall viscous sublayer is confirmed to be resolved
¹²³ with at least 2 grid points within one viscous wall unit of the boundary at all times ($\delta_v = \nu/u^*$,
¹²⁴ where $u^* = \sqrt{|\boldsymbol{\tau}|/\rho_o}$, and $|\boldsymbol{\tau}|$ is the magnitude of the bottom stress).

¹²⁵ *b. Description of simulation evolution*

¹²⁶ The full set of simulations considered here span a wide-range of slope angles, interior stratifi-
¹²⁷ cation, and slope Burger numbers (as listed in table 1). It is however useful to begin with a brief
¹²⁸ qualitative description of several representative simulations. Figure 2 shows the evolution of sim-
¹²⁹ ulation SI-1, which has an initial slope Burger number of $S_\infty = 0.6$, indicating a moderately-steep
¹³⁰ regime where symmetric instability is expected (Wenegrat et al. 2018). The simulation begins with
¹³¹ a barotropic interior flow along the slope (V_∞), which generates a downslope Ekman flow ($u < 0$)
¹³² within approximately an inertial period in response to the associated along-slope bottom stress.
¹³³ This Ekman flow advects buoyant water down the slope in a thin near boundary Ekman layer,
¹³⁴ which generates convective mixing that destroys stratification, producing a bottom boundary layer
¹³⁵ which grows to ~ 50 m thickness after 15 days.

136 The destruction of stratification by the downslope Ekman transport is also associated with
137 a boundary flux of Ertel potential vorticity (PV, BenthuySEN and Thomas 2012), defined as
138 $q = \omega \cdot \nabla b_T$, where ω is the total absolute vorticity vector. This leads to a BBL characterized
139 by $fq < 0$ (which can be seen in the first several days of the simulation), stable vertical stratifica-
140 tion, and $f(f + \partial v / \partial \hat{x}) > 0$, a state which is unstable to symmetric instability (Haine and Marshall
141 1998; Thomas et al. 2013). In classic 1D theory, or in a simulation where submesoscale instabil-
142 ities were not resolved, this evolution would continue, with convective turbulence deepening the
143 well-mixed boundary layer until an arrested Ekman state was achieved, or the flow relaminarized
144 (MacCready and Rhines 1991, 1993; Ruan et al. 2019). Here however the state of $fq < 0$ gives rise
145 to rapidly growing symmetric instability (figure 3), which reaches finite amplitude within several
146 days, and returns the boundary layer to $q \approx 0$ (figure 2). Also evident in figure 3 are secondary
147 Kelvin-Helmholtz instabilities, generated by the sheared SI overturning cells, which enhance the
148 boundary layer dissipation (Taylor and Ferrari 2009, and section 4). These conditions, where
149 an Ekman buoyancy flux pushes the boundary layer towards $fq < 0$ and symmetric instabilities
150 return the boundary layer to the point of marginal stability, $q \approx 0$, is a regime known from the sur-
151 face boundary layer literature as ‘forced symmetric instability’ (TF10; Thomas and Taylor 2010;
152 Thomas et al. 2013), newly identified here as a feature of the BBL.

153 A useful diagnostic for determining the fastest growing instability type in each portion of
154 the domain comes from linear theory, developed in Thomas et al. (2013). Assuming a flow
155 that is in approximate geostrophic balance, an instability angle can be defined as $\phi_{Ri_b} =$
156 $\tan^{-1}(-|\partial b / \partial \hat{x}|^2 / f^2 N^2)$, such that growing instabilities will occur when ϕ_{Ri_b} is smaller than a
157 critical angle of $\phi_c = \tan^{-1}(-(f + \partial v_g / \partial \hat{x}) / f)$ (Thomas et al. 2013). Symmetric modes dominate
158 for $-90^\circ < \phi_{Ri_b} < -45^\circ$, growing through vertical shear production, and when $-45^\circ < \phi_{Ri_b} < \phi_c$
159 mixed symmetric-centrifugal modes grow via both lateral and vertical shear production. When

the stratification becomes unstable ($N^2 < 0$, $\phi_{Ri_b} < -90^\circ$), the fastest growing mode will either be a gravitational instability or a mixed gravitational-symmetric mode depending on the relative magnitude of the vertical buoyancy production and shear production (see Thomas et al. 2013, appendix). To reduce noise associated with calculating these quantities from the high-resolution numerical model we first smooth the stratification and buoyancy gradients to $\Delta x \approx 14$ m and $\Delta z \approx 3$ m resolution (which are much smaller than the vertical and horizontal scales of the instabilities themselves), and use across-slope averaged profiles of the geostrophic vertical relative vorticity to determine ϕ_c and the transition between gravitational and mixed gravitational-symmetric modes (see equation 41 of Thomas et al. 2013). The resulting estimate of ϕ_{Ri_b} for simulation SI-1 is shown in figure 4, with the color scale indicating the primary instability type, illustrating how most of the BBL is dominated by symmetric instability. Near the lower-boundary regions of gravitational and mixed gravitational-symmetric instabilities are evident, associated with the near-boundary convective layer (section 3c). In the center of the domain buoyancy advection by the SI overturning cells generates a plume of gravitationally unstable fluid which extends towards the top of the boundary layer.

A similar evolution is evident in simulation CI-1, which is configured with the same interior stratification, but a steeper slope, such that the slope Burger number is $S_\infty = 1.6$ (table 1). Following the same basic evolution, a downslope Ekman flow develops rapidly at the beginning of the simulation, generating a growing BBL that is associated with reduced stratification and low PV (figure 5). Early in this run $f(f + \partial v / \partial \hat{x}) < 0$, indicative of centrifugal instability (Haine and Marshall 1998). Later, as the boundary layer adjusts to $q \approx 0$ the flow becomes inertially stable, but the instability continues to gain energy primarily through lateral shear production (section 4), in what can be considered as a mixed SI/CI mode (Wenegrat et al. 2018).

183 Notable differences between the two runs include a more rapid shut-down of the cross-slope
 184 flow, and a faster growing boundary layer that remains more stratified, in simulation CI-1 com-
 185 pared to SI-1. It will be shown below that these results all follow directly as a consequence of
 186 the increased slope-angle, and hence slope Burger number, of CI-1. As in SI-1, overturning cells
 187 are evident in the cross-frontal snapshot of CI-1 (figure 6). These instabilities are of a mixed
 188 centrifugal-symmetric type (figure 7), growing primarily through energy extracted from the lateral
 189 shear of the geostrophic flow (section 4) — enhanced in CI-1 due to the steeper slope angle, which
 190 allows the slope-normal shear to project more efficiently on the horizontal — with additional con-
 191 tributions from vertical shear production. The finite amplitude CI thus acts similarly to the SI
 192 modes, bringing the boundary layer PV back to zero in what can be considered a *forced centrififu-*
 193 *gal instability*, and it will be shown below that indeed the boundary layer evolution is governed by
 194 the same essential dynamics, regardless of whether the instabilities are predominantly of the SI or
 195 CI type.

196 3. Theory of forced SI/CI in the BBL

197 To understand the evolution of the boundary layer shown in figures 2 - 7 it is useful to take the
 198 mean of the governing equations (1)-(4),

$$\frac{\partial \langle u \rangle}{\partial t} - f \langle v \rangle = \langle b \rangle \theta - \frac{\partial \langle u' w' \rangle}{\partial z} + v \frac{\partial^2 \langle u \rangle}{\partial z^2}, \quad (7)$$

$$\frac{\partial \langle v \rangle}{\partial t} + f \langle u \rangle = - \frac{\partial \langle v' w' \rangle}{\partial z} + v \frac{\partial^2 \langle v \rangle}{\partial z^2}, \quad (8)$$

$$f \langle v \rangle \theta = - \frac{1}{\rho_o} \frac{\partial \langle p \rangle}{\partial z} + b - \frac{\partial \langle w' w' \rangle}{\partial z}, \quad (9)$$

$$\frac{\partial \langle b \rangle}{\partial t} + N_\infty^2 \theta \langle u \rangle = - \frac{\partial \langle w' b' \rangle}{\partial z} + \kappa \frac{\partial^2 \langle b \rangle}{\partial z^2}, \quad (10)$$

199 where $\langle \cdot \rangle$ denotes the average over the across-slope (x) direction, and primes indicate departure
 200 from the average. Note that for notational simplicity here, and in the remainder of the manuscript,

we make the small-angle approximation ($\cos \theta \approx 1$, $\sin \theta \approx \theta$), which is satisfied by most oceanographically relevant slope angles. Example profiles of the dominant terms in the across and along-slope momentum budget for simulation SI-1 are shown in figure 8, showing how buoyancy perturbations and momentum flux divergences are primarily balanced at subinertial timescales by Coriolis accelerations. The along-slope momentum balance is similar to the turbulent Ekman balance found for the surface boundary layer in TF10, and explains the vertical structure of the cross-slope flow shown in figures 2 and 5, where downslope Ekman flow in a thin near-boundary layer sits below an across-slope secondary circulation driven by the mixing of geostrophic momentum (TF10; Wenegrat and McPhaden 2016).

In the following sections we show how the SI/CI modes bringing the boundary layer to the state of marginal stability, where $q \approx 0$, can be used to constrain many aspects of the boundary layer evolution. We emphasize that significant portions of this are an adaptation of the work of TF10 to the slope, however in the interest of parsimony we will not explicitly note every connection with that work.

$a.$ Potential Vorticity

In the rotated coordinate system the mean PV can be written as,

$$\langle q \rangle = f \frac{\partial \langle b \rangle}{\partial z} + f N_\infty^2 + \frac{\partial \langle \zeta' b' \rangle}{\partial z} - N_\infty^2 \theta \frac{\partial \langle v \rangle}{\partial z}, \quad (11)$$

where $\zeta = \partial v / \partial x$ is the slope normal relative vorticity in the 2D configuration considered here.

The PV evolves following,

$$\frac{\partial \langle q \rangle}{\partial t} + \frac{\partial \langle J^z \rangle}{\partial z} = 0, \quad (12)$$

where J^z is the slope-normal component of the PV flux,

$$\mathbf{J} = q \mathbf{u} - \omega \kappa \nabla^2 b + \nabla b_T \times v \nabla^2 \mathbf{u}. \quad (13)$$

220 Outside of thin viscous/diffusive layers near the boundary, the PV evolution can be approximated
221 by,

$$\frac{\partial \langle q \rangle}{\partial t} + \frac{\partial \langle q' w' \rangle}{\partial z} \simeq 0. \quad (14)$$

222 Using (11) in (14) then gives,

$$f \frac{\partial}{\partial t} \frac{\partial \langle b \rangle}{\partial z} + \frac{\partial}{\partial t} \frac{\partial \langle \zeta' b' \rangle}{\partial z} - N_\infty^2 \theta \frac{\partial}{\partial t} \frac{\partial \langle v \rangle}{\partial z} + \frac{\partial \langle q' w' \rangle}{\partial z} \simeq 0. \quad (15)$$

223 Integrating in the slope-normal direction,

$$f \frac{\partial}{\partial t} \langle b \rangle + \frac{\partial}{\partial t} \langle \zeta' b' \rangle - N_\infty^2 \theta \frac{\partial}{\partial t} \langle v \rangle + \langle q' w' \rangle \simeq C(t), \quad (16)$$

224 where C is a constant of integration that depends only on time. The perturbation quantities and PV
225 flux go to 0 above the BBL, hence it must be the case that $C(t) = 0$.

226 Using the mean buoyancy equation (10), the PV flux can then be written as¹,

$$\langle q' w' \rangle \simeq N_\infty^2 \theta \left(\frac{\partial \langle v \rangle}{\partial t} + f \langle u \rangle \right) + f \frac{\partial \langle w' b' \rangle}{\partial z} - \frac{\partial \langle \zeta' b' \rangle}{\partial t}. \quad (17)$$

227 For subinertial motions the last-term on the right-hand side is small relative to the first two terms
228 (following the scaling analysis given in TF10, their appendix), and hence it can be neglected,

$$\langle q' w' \rangle \simeq N_\infty^2 \theta \left(\frac{\partial \langle v \rangle}{\partial t} + f \langle u \rangle \right) + f \frac{\partial \langle w' b' \rangle}{\partial z}. \quad (18)$$

229 Substituting for the term in parentheses using the mean along-slope momentum balance (8) gives,

$$\langle q' w' \rangle \simeq -N_\infty^2 \theta \frac{\partial \langle v' w' \rangle}{\partial z} + f \frac{\partial \langle w' b' \rangle}{\partial z}. \quad (19)$$

¹Throughout we ignore the molecular diffusive fluxes of buoyancy as they tend to be small relative to other terms. Formally this can be posed (see appendix) as the requirement that $f \kappa (1 + S_\infty^2) / u^{*2} \theta \ll 1$, ie the Thorpe transport (Thorpe 1987) is small relative to the Ekman transport, such that advective and resolved turbulent fluxes dominate the diffusive flux. This is generally true, with the exception being the late-time evolution of the large slope Burger number cases, which undergo significant Ekman arrest (section 5), such that $u^* \rightarrow 0$ and diffusive fluxes can become important. We consider this as somewhat artificial, both due to the enhanced diffusivity used here and the long integration times. Regardless, the cumulative errors due to this approximation remain small in these few cases, hence diffusive terms can be safely ignored.

230 For the PV to remain steady in the BBL, the flux must be non-divergent over the BBL (see equation
 231 14), therefore $-N_\infty^2 \theta \langle v' w' \rangle + f \langle w' b' \rangle$ is at most a linear function of the slope-normal distance
 232 (figure 9).

233 *b. Scaling for H, the height of the low PV layer*

234 Once the instabilities have reached finite amplitude in the numerical simulations the boundary
 235 layer stratification does not evolve significantly in time, ie. $\partial b / \partial t$ is independent of z . Thus,
 236 integrating the mean buoyancy equation (10) over the boundary layer height $H(t)$ from the bottom
 237 (again ignoring the small diffusive fluxes of buoyancy),

$$H \frac{\partial \langle b \rangle}{\partial t} \simeq -\langle w' b' \rangle_{z=H} - N_\infty^2 \theta \int_0^H \langle u \rangle dz. \quad (20)$$

238 For the case of a sloping bottom the depth-integrated buoyancy can only be in steady-state when
 239 the cross-slope advection exactly balances the buoyancy flux divergence (Thorpe 1987). As the
 240 buoyancy perturbation enters the momentum balance, through (7), this implies that there is not
 241 necessarily a steady-state solution for any arbitrary Ekman transport, unlike in the surface bound-
 242 ary layer. However, by integrating (7), (8) and (10) in the slope-normal direction, it is possible to
 243 combine the across and along slope momentum equations to give an approximate equation for the
 244 across-slope transport (see appendix, and Brink and Lentz 2010)²,

$$\int_0^H \langle u \rangle dz \simeq -\frac{1}{f(1+S_\infty^2)} \left[\frac{\langle \tau^y \rangle}{\rho_o} + \frac{\theta}{f} \langle w' b' \rangle_{z=H} \right], \quad (21)$$

245 where $\tau^y = \rho_o v \partial v / \partial z|_{z=0}$ is the along-slope bottom stress. The cross-slope transport is therefore
 246 given by the BBL Ekman transport, modified to account for the reduction of the Ekman flow by
 247 buoyancy forces in the across-slope momentum budget (Brink and Lentz 2010).

²We ignore entrainment fluxes of momentum at $z = H$ for clarity, as they do not contribute significantly in the numerical simulations.

²⁴⁸ Using (21) in (20) gives,

$$H \frac{\partial \langle b \rangle}{\partial t} \simeq (1 + \alpha) EBF_s, \quad (22)$$

²⁴⁹ where we have introduced the slope Ekman Buoyancy Flux,

$$EBF_s = \frac{\langle \tau^y \rangle}{\rho_o f} \frac{N_\infty^2 \theta}{1 + S_\infty^2}, \quad (23)$$

²⁵⁰ and where $\alpha = -\langle w' b \rangle_{z=H} (1 + S_\infty^2)^{-1} EBF_s^{-1}$ is an entrainment factor accounting for the turbulent
²⁵¹ buoyancy flux at $z = H$. Practically this term is only important in the simulations dominated by
²⁵² convection, and can otherwise be ignored (section 3c).

²⁵³ The rate of change of buoyancy can be related to the PV flux outside of the near-boundary
²⁵⁴ diffusive layer by using (10), (18), and noting that $\partial \langle v \rangle / \partial t \simeq -f^{-1} \theta \partial \langle b \rangle / \partial t$ (appendix), such
²⁵⁵ that,

$$\langle q' w' \rangle \simeq -f(1 + S_\infty^2) \frac{\partial \langle b \rangle}{\partial t}. \quad (24)$$

²⁵⁶ Then, defining $H(t)$ as the location where the PV flux vanishes, $\langle J^z \rangle_{z=H} = 0$, and integrating (12)
²⁵⁷ vertically gives,

$$\frac{\partial}{\partial t} \int_0^{H(t)} \langle q \rangle dz - \frac{\partial H}{\partial t} \langle q \rangle_{z=H} \simeq -(1 + \alpha) (1 + S_\infty^2) \frac{f EBF_s}{H}, \quad (25)$$

²⁵⁸ where we have used (22) and (24) to write $\langle J^z \rangle_{z=0} \simeq -(1 + \alpha)(1 + S_\infty^2)fEBF_s/H$, as the PV flux
²⁵⁹ is assumed constant through the BBL. The rate of change of the integrated boundary layer PV
²⁶⁰ will be small when convective mixing or symmetric/centrifugal instabilities cause $\langle q \rangle \approx 0$ through
²⁶¹ most of the BBL. Setting $\langle q \rangle_{z=H} = fN_\infty^2$, reflecting the entrainment of interior PV, then gives an
²⁶² equation for the rate of change of the thickness of the low PV layer,

$$H \frac{\partial H}{\partial t} \simeq (1 + \alpha) (1 + S_\infty^2) \frac{EBF_s}{N_\infty^2}. \quad (26)$$

²⁶³ This can be further simplified as,

$$H \frac{\partial H}{\partial t} = (1 + \alpha) \frac{\langle \tau^y \rangle \theta}{\rho_o f}, \quad (27)$$

264 showing how the time evolution of the boundary layer thickness differs from the expectation for
265 upright convection — growing faster by a factor of $1 + S_\infty^2$ (Deardorff et al. 1969) — and depends
266 only weakly on the interior stratification and slope Burger number (through the entrainment fluxes
267 and the bottom stress as discussed in section 5). The accuracy of the boundary layer height pre-
268 dicted by integrating (27) can be seen by comparing the thick black line in the bottom panels of
269 figures 2 and 5 to the depth of the simulated low PV layer.

270 *c. Scaling for h , the height of the convective layer*

271 During SI/CI the boundary layer divides into two regions. Near the lower boundary the strati-
272 fication remains low and turbulent buoyancy fluxes act to increase the eddy kinetic energy — in
273 what is termed the convective layer (TF10) — above which lies a stratified region where in-
274 stabilities are active. In some conditions the convective layer can fill the majority of the boundary
275 layer, allowing upright convection to persist even in conditions that otherwise appear conducive to
276 SI/CI, and it is therefore useful to determine a diagnostic equation for the height of the convective
277 layer, $h(t)$.

278 In the surface boundary layer the convective layer depth is generally defined as the location
279 where the total vertical buoyancy flux is zero (TF10), however in our simulations we find that this
280 definition does not usefully partition the boundary layer into regions with distinct dynamics. The
281 reason for this can be seen clearly by decomposing the slope-normal buoyancy flux by across-slope
282 wavenumber (figure 9, panel b). Slope-normal buoyancy fluxes with across-slope wavelengths
283 $\lambda_x > 100$ m are associated with the SI/CI overturning cells, and are positive through a significant
284 portion of the lower boundary layer, whereas fluxes associated with smaller scale turbulent motions
285 ($\lambda_x < 100$ m) decay rapidly away from the boundary. The convective layer depth, as commonly
286 defined, is therefore largely determined by the overturning cells of the instability themselves in

these simulations, and hence does not discriminate regions of the boundary layer where SI/CI is active or not. Detailed exploration of why the instability cells are slightly inclined from isopycnal surfaces, and hence generate buoyancy fluxes is beyond the scope of the present work (see related work by Grisouard 2018). However we note that the regions of positive buoyancy fluxes by SI/CI are largely compensated by negative buoyancy fluxes in the upper portion of the boundary layer, such that shear production still dominates the total instability energetics (section 4).

Given this, we take an alternate definition of the convective layer height as the location at which the small-scale turbulent slope-normal buoyancy fluxes equal 0. To do this we decompose the total slope-normal buoyancy fluxes into contributions from SI/CI and turbulent motions, denoted as $\langle w'b' \rangle^I$ and $\langle w'b' \rangle^T$ respectively. Then, integrating the mean buoyancy equation (10) to the height of the convective layer, h — where $\langle w'b' \rangle^T = 0$ by definition — and again ignoring small diffusive fluxes, gives,

$$\int_0^h \frac{\partial \langle b \rangle}{\partial t} dz \simeq -N_\infty^2 \theta \int_0^h \langle u \rangle dz - \langle w'b' \rangle_{z=h}^I. \quad (28)$$

Recalling that the rate of change of buoyancy is independent of z in the boundary layer, (22) implies,

$$\frac{h}{H} (1 + \alpha) EBF_s \simeq -N_\infty^2 \theta \int_0^h \langle u \rangle dz - \langle w'b' \rangle_{z=h}^I. \quad (29)$$

The vertical integral of the cross-slope velocity can be re-written as (see appendix),

$$\int_0^h \langle u \rangle dz \simeq -\frac{1}{f(1 + S_\infty^2)} \left[\langle v'w' \rangle|_{z=h} + \frac{\langle \tau^y \rangle}{\rho_o} + \frac{\theta}{f} \langle w'b' \rangle_{z=h}^I \right], \quad (30)$$

i.e. the cross-slope transport over the layer is proportional to the divergence of the along-slope momentum flux plus a contribution from the buoyancy flux divergence (and where we have ignored small diffusive fluxes of momentum at $z = h$). Thus,

$$\frac{h}{H} (1 + \alpha) EBF_s \simeq \frac{N_\infty^2 \theta}{f(1 + S_\infty^2)} \langle v'w' \rangle|_{z=h} + EBF_s - \frac{1}{1 + S_\infty^2} \langle w'b' \rangle_{z=h}^I. \quad (31)$$

305 Solving this equation directly for h using numerical estimates³ of H , $\langle v'w' \rangle_{z=h}$, and $\langle w'b' \rangle^I_{z=h}$ (306 defined using a cutoff wavelength of $\lambda_x = 100$ m) shows excellent agreement with the true convective 307 layer depth across all simulations ($r^2 = 0.98$).

308 To close this equation for diagnostic purposes it is necessary to estimate the eddy momentum 309 and buoyancy flux terms. To do this we assume that the along-front turbulent velocity scale goes 310 like the change in geostrophic velocity over the convective layer $v' \sim h\partial v_g / \partial z$, the buoyancy 311 perturbation scales as the change in total buoyancy over the convective layer $b' \sim hN^2$, and the 312 vertical velocity scales with the convective velocity $w' \sim (EBF_s h)^{1/3}$ (as in TF10). The $q \approx 0$ 313 condition provides a constraint on the perturbation buoyancy gradient in the boundary layer, which 314 under the assumption of linear variation of buoyancy through the boundary layer (see for example 315 figure 8), can be written following Allen and Newberger (1998, their equation 2.53) as,

$$\frac{\partial \langle b \rangle}{\partial z} \simeq -\frac{N_\infty^2}{1 + S_\infty^2}. \quad (32)$$

316 Noting that the geometry of the problem gives $\partial \langle b \rangle / \partial \hat{x} = -\theta \partial \langle b \rangle / \partial z$, the thermal wind shear 317 can then be written as $\partial \langle v_g \rangle / \partial \hat{z} \simeq N_\infty^2 \theta / f(1 + S_\infty^2)$. Using these relationships and scalings, the 318 equation governing the convective layer depth can be written,

$$\left(\frac{h}{H}\right)^4 - C^3 \left(\frac{u^{*2}}{\Delta v_g^2} \cos \gamma\right)^2 \left[1 - (1 + \alpha) \frac{h}{H}\right]^3 = 0, \quad (33)$$

319 where C is a constant with best estimate determined from fitting the numerical simulations of 320 $C = 7.9$ (figure 10), $\gamma = \cos^{-1}(\tau^y / |\tau|)$ is the angle of the bottom stress relative to the along-slope 321 direction, and $\Delta v_g = HN^2 \theta / f(1 + S_\infty^2)$ is the change in geostrophic velocity over the boundary

³As a practical matter the PV flux calculated from a numerical model is often a noisy quantity, which can make directly determining the height of the low PV layer difficult. In the few places necessary we instead take the simplifying approach of estimating H from the numerical simulations as the height at which $\langle q \rangle = 0.5fN_\infty^2$, which we find provides a reasonable estimate of where $\langle q'w' \rangle \approx 0$. This definition differs slightly from that used in the derivation of (27), likely due to diffusive fluxes at the top of the boundary layer not considered in the theory. Alternate methods of estimating H from the numerical simulations were tested and found to only lead to minor quantitative changes.

322 layer height. Aside from slight differences in the empirical coefficient, this equation is the same
323 as for the convective depth in the surface boundary layer in the case of downfront winds and no
324 surface buoyancy loss (TF10; Thomas et al. 2013). Alternate definitions of the cutoff wavelength,
325 λ_x , were tested and found to lead to only minor quantitative changes in the best-fit coefficient.

326 The convective layer height is therefore controlled by the term $u^*/\Delta v_g$, the ratio of the friction
327 velocity to the change in geostrophic velocity over the BBL. An alternate expression of this utilizes
328 the slope Monin-Obukhov length (Ruan et al. 2019),

$$L_s = \frac{u^{*3}}{\mathcal{K} EBF_s}, \quad (34)$$

329 where $\mathcal{K} = 0.4$ is the von Kármán constant, such that $u^*/\Delta v_g \approx \mathcal{K} L_s/H$ (assuming $\gamma \approx 0$). Thus,
330 when $L_s/H \ll 1$ the first term in (33) dominates, and the convective layer depth goes to 0. When
331 $L_s/H \gg 1$ only the second term in (33) contributes, and the convective layer fills the boundary
332 layer outside an entrainment layer near the boundary layer top, such that $h \approx H/(1 + \alpha)$. An
333 example of this latter case is shown in figure 11 for simulation CONV-1, where $L_s/H \gg 1$, and
334 SI/CI are absent and the boundary layer is instead characterized by gravitational instability (figure
335 12).

336 Conditions of $f q < 0$ are therefore not independently sufficient for SI/CI in the BBL, and it is
337 additionally necessary that $h/H \ll 1$. This final criteria is satisfied when the change in geostrophic
338 velocity over the boundary layer height is much larger than the friction velocity (or equivalently
339 $L_s/H \ll 1$), similar to the criteria for wind-forced SI in the surface boundary layer (Thomas et al.
340 2013). However, unlike the surface boundary layer case, in the BBL these two quantities are not
341 independent, as increasing Δv_g acts to decrease the bottom stress, discussed further in section 5.

342 **4. Energetics**

343 In the slope-coordinate system the eddy kinetic energy (EKE) budget is,

$$\frac{\partial \langle k \rangle}{\partial t} = \underbrace{\langle w'b' \rangle + \langle u'b' \rangle}_{VBP} \theta - \underbrace{\langle v'w' \rangle}_{SP} \frac{\partial \langle v \rangle}{\partial z} - \underbrace{\langle u'w' \rangle}_{SP} \frac{\partial \langle u \rangle}{\partial z} - \underbrace{\frac{\partial}{\partial z} \left(\langle w'k' \rangle + \langle w'p' \rangle - v \frac{\partial \langle k \rangle}{\partial z} \right)}_{TRANSPORT} - \underbrace{\varepsilon}_{DISS}, \quad (35)$$

344 where $k = (u'^2 + v'^2 + w'^2)/2$ is the EKE, $\varepsilon = v \langle s'_{i,j} s'_{i,j} \rangle$ is the dissipation rate, and $s'_{i,j} =$
345 $(\partial u'_i / \partial x_j + \partial u'_j / \partial x_i)/2$ is the strain tensor. Terms in the budget are, from left to right, the vertical
346 buoyancy production (VBP, which involves both slope-normal and across-slope fluxes), shear pro-
347 duction (SP), transport of EKE (TRANSPORT), and dissipation of eddy kinetic energy (DISS).

348 Note that the slope-normal direction projects on both the horizontal and vertical directions, hence
349 the slope-normal shear production term (SP) includes contributions from both lateral shear pro-
350 duction ($LSP = -\langle \hat{u}'\hat{u}' \rangle \cdot \partial \langle \hat{u} \rangle / \partial \hat{x}$) and vertical shear production ($VSP = -\langle \hat{u}'\hat{w}' \rangle \cdot \partial \langle \hat{u} \rangle / \partial \hat{z}$) com-
351 ponents (recalling that the hat notation indicates terms evaluated in the standard non-rotated frame,
352 figure 1).

353 To further simplify the budget, the shear production can be decomposed into geostrophic and
354 ageostrophic components. The governing equations for the mean shear (assuming sub-inertial
355 timescales, and dropping viscous terms)⁴ are,

$$-f \frac{\partial \langle v \rangle}{\partial z} \simeq \frac{\partial \langle b \rangle}{\partial z} \theta - \frac{\partial^2 \langle u'w' \rangle}{\partial z^2}, \quad (36)$$

$$f \frac{\partial \langle u \rangle}{\partial z} \simeq -\frac{\partial^2 \langle v'w' \rangle}{\partial z^2}. \quad (37)$$

356 ⁴Note that when considering the horizontal momentum equations the rate of change of buoyancy still influences the along-slope momentum balance, and hence it is necessary to retain the rate of change terms, as discussed in the appendix. However here, where we consider the equations governing the mean slope-normal shear, the assumptions that momentum evolves on subinertial timescales and that $\partial^2 \langle b \rangle / \partial z \partial t \approx 0$, together allow the rate of change terms to be neglected.

³⁵⁷ Using these, the SP can be written as,

$$SP \simeq \frac{1}{f} \frac{\partial}{\partial z} \left(-\langle v' w' \rangle \frac{\partial \langle u' w' \rangle}{\partial z} + \langle u' w' \rangle \frac{\partial \langle v' w' \rangle}{\partial z} \right) + \underbrace{\frac{\langle v' w' \rangle}{f} \frac{\partial \langle b \rangle}{\partial z}}_{GSP_s} \theta. \quad (38)$$

³⁵⁸ The turbulent fluxes go to 0 at the boundary and in the interior, hence the first term integrates to
³⁵⁹ 0, leaving only the final term involving the slope-normal perturbation buoyancy gradient. Noting
³⁶⁰ that $\partial v_g / \partial z = -f^{-1} \theta \partial b / \partial z$, we denote this as the slope Geostrophic Shear Production

$$GSP_s = -\langle v' w' \rangle \frac{\partial \langle v_g \rangle}{\partial z}. \quad (39)$$

³⁶¹ The portion of the shear production which contributes to the vertically integrated EKE tendency
³⁶² thus reduces to a single term, involving the slope-normal momentum fluxes extracting energy
³⁶³ from the slope-normal shear of the geostrophic flow. The distinction between centrifugal and
³⁶⁴ symmetric modes — defined by their primary energy source of lateral or vertical shear production,
³⁶⁵ respectively — can therefore be seen to be somewhat artificial in the BBL, where instabilities will
³⁶⁶ smoothly transition between SI/CI modes, and will often involve mixed symmetric-centrifugal
³⁶⁷ modes with energy extraction from both the vertical and horizontal shear of the geostrophic flow.
³⁶⁸ However, if desired the GSP_s can also be expressed in terms of standard vertical and lateral shear
³⁶⁹ production terms,

$$GSP_s = \underbrace{-\langle v' \hat{w}' \rangle \frac{\partial \langle v_g \rangle}{\partial \hat{z}}}_{VGSP} - \underbrace{-\langle v' \hat{u}' \rangle \frac{\partial \langle v_g \rangle}{\partial \hat{x}}}_{LGSP}. \quad (40)$$

³⁷⁰ The slope Geostrophic Shear Production is thus similar to the energy source for SI in the surface
³⁷¹ boundary layer (VGSP), but also includes the contribution of energy extraction from the lateral
³⁷² geostrophic shear (LGSP).

³⁷³ The relative importance of these energy sources can be estimated using the fact that the fastest
³⁷⁴ growing mode is aligned along isopycnals (Thomas et al. 2013), which have slope $\partial z / \partial x|_\rho \approx$

375 $-\theta S_\infty^{-2}$ when $q \approx 0$ (Allen and Newberger 1998), the ratio of *LGSP* to *VGSP* will be,

$$\frac{LGSP}{VGSP} \sim -\left(\frac{\partial z}{\partial x}\Big|_\rho\right)^{-1} \theta \simeq S_\infty^2. \quad (41)$$

376 The same result can also be derived directly from the definition of the PV, which, assuming that
377 the flow is in approximate geostrophic balance, can be written,

$$q \simeq fN^2 \left(1 + Ro_b - \frac{1}{Ri_b}\right), \quad (42)$$

378 where $Ro_b = f^{-1} \partial v_g / \partial \hat{x}$ and $Ri_b = N^2 (\partial v_g / \partial \hat{z})^{-2}$ are the balanced Rossby and Richardson num-
379 ber, respectively. The ratio of the last two terms in this equation (ie. $-Ro_b/Ri_b^{-1} = -Ro_b Ri_b$) thus
380 determines whether the PV is vortically low (associated with CI), or baroclinically low (associated
381 with SI, Thomas 2008). Using (32), this can be approximated by,

$$-Ro_b Ri_b \simeq S_\infty^2. \quad (43)$$

382 Thus, both the energetics and PV indicate that centrifugal-type instabilities are expected to occur
383 when the interior slope Burger number exceeds 1, and symmetric-type instabilities will be found
384 when $S_\infty < 1$. An example of this is shown in figure 13, where for simulation CI-1 ($S_\infty > 1$) lateral
385 shear production dominates outside the thin near-boundary convective layer, whereas simulation
386 SI-1 ($S_\infty < 1$) is everywhere dominated by vertical shear production.

387 Importantly, while the SI/CI modes grow via GSP_s , much of the total energy extracted from
388 the geostrophic flow via shear production is balanced directly by dissipation. An example of this
389 is shown in figure 14 for simulation SI-1, where the rate of change of EKE is a small residual
390 between the near compensation of shear production and dissipation. It is therefore of interest to
391 constrain the magnitude and vertical structure of the combined EKE production terms, as these set
392 the dissipation rate in the boundary layer. In the surface boundary layer these follow directly from
393 the PV flux equation (TF10; Thomas and Taylor 2010), however, in the BBL case a few additional

³⁹⁴ steps are necessary. First, consider the eddy potential energy (EPE) equation, ignoring vertical
³⁹⁵ transport terms for simplicity,

$$\frac{\partial}{\partial t} \left(\frac{\langle b'^2 \rangle}{2N_\infty^2} \right) = \underbrace{-\langle w'b' \rangle - \langle u'b' \rangle \theta}_{-VBP} - \underbrace{\frac{\langle w'b' \rangle}{N_\infty^2} \frac{\partial \langle b \rangle}{\partial z}}_{MPE-EPE} - \underbrace{\frac{\kappa}{N_\infty^2} \left\langle \frac{\partial b'}{\partial z} \frac{\partial b'}{\partial z} \right\rangle}_{DISS_b}. \quad (44)$$

³⁹⁶ The first term on the right-hand side is the negative of the vertical buoyancy production term,
³⁹⁷ representing the loss of eddy potential energy to eddy kinetic energy, the second term is the con-
³⁹⁸ version between mean and eddy potential energy (MPE-EPE), and the final term gives the rate of
³⁹⁹ irreversible mixing of buoyancy (DISS_b).

⁴⁰⁰ The numerical simulations show that, when in the forced-SI/CI regime, both the rate of change
⁴⁰¹ of EPE and DISS_b are small. Hence the EPE budget can be approximated as,

$$0 \simeq -\langle w'b' \rangle - \langle u'b' \rangle \theta - \frac{\langle w'b' \rangle}{N_\infty^2} \frac{\partial \langle b \rangle}{\partial z}. \quad (45)$$

⁴⁰² Using (32), this gives,

$$\frac{\langle w'b' \rangle}{1 + S_\infty^2} \simeq \underbrace{\langle w'b' \rangle + \langle u'b' \rangle \theta}_{VBP}. \quad (46)$$

⁴⁰³ Physically this states that in the limit where both the rate of change and dissipation of EPE
⁴⁰⁴ are small, conversions between eddy potential and kinetic energy are balanced by conversions
⁴⁰⁵ between mean and eddy potential energy. Finally, using (32) the GSP_s can be expressed as
⁴⁰⁶ $GSP_s \simeq -\langle v'w' \rangle N_\infty^2 \theta / f(1 + S_\infty^2)$, allowing the EKE budget to be approximated as,

$$\frac{\partial \langle k \rangle}{\partial t} \simeq \frac{1}{1 + S_\infty^2} \left[\langle w'b' \rangle - \langle v'w' \rangle \frac{N_\infty^2 \theta}{f} \right] - \varepsilon. \quad (47)$$

⁴⁰⁷ From the PV flux equation (19) the first term on the right-hand side of (47) is a linear function
⁴⁰⁸ of z , with maximum value given by EBF_s (figure 9). In the case that the rate of change of EKE is
⁴⁰⁹ small, this implies that the dissipation must also be a linear function of z , with magnitude set by

410 the slope Ekman buoyancy flux (figure 15),

$$\varepsilon_{SI} \approx \begin{cases} EBF_s \left(1 - \frac{z}{H}\right), & \text{if } z \leq H \\ 0, & \text{otherwise.} \end{cases} \quad (48)$$

411 The vertically integrated dissipation from SI/CI in the BBL will therefore go as $(H/2)EBF_s$. A
412 comparison of the depth-integrated production terms, first term in (47), to the parameterized depth-
413 integrated dissipation is shown in figure 15c. The agreement is excellent across all simulations,
414 although the dissipation is overestimated by approximately 10%, likely due to production terms
415 that go to zero near the lower boundary more smoothly than predicted by the piecewise approxi-
416 mation given by (48). A similar result for SI in the surface boundary layer has proven useful in ex-
417 plaining observations of enhanced turbulent dissipation at symmetrically unstable fronts (D'Asaro
418 et al. 2011; Thomas et al. 2016), and for the development of parameterizations of unresolved SI
419 turbulence (Bachman et al. 2017).

420 5. Symmetric/centrifugal instability and Ekman buoyancy arrest

421 Above it is shown that during the Ekman adjustment process of the boundary layer the flow
422 quickly becomes unstable to SI/CI, which grow to finite amplitude and begin to modify the dy-
423 namical evolution of the boundary layer. It is therefore of interest to consider how the presence
424 of these instabilities modifies the classic picture of Ekman buoyancy arrest, where 1D theory pre-
425 dicted that the development of thermal wind shear in the BBL will eventually bring the along-slope
426 bottom velocity (and consequently the along-slope bottom stress) to zero, shutting down the cross-
427 slope Ekman buoyancy flux (MacCready and Rhines 1991, 1993; Brink and Lentz 2010). The most
428 obvious modification to the Ekman arrest process by SI/CI is through the enhanced stratification
429 of the boundary layer necessary to bring the PV to the point of marginal stability ($q \approx 0$). As
430 noted by Allen and Newberger (1998) this modifies the depth of the BBL necessary to achieve full

431 Ekman arrest,

$$H_a = \frac{V_\infty f(1 + S_\infty^2)}{N_\infty^2 \theta}, \quad (49)$$

432 ie. increasing the arrested BBL height by a factor of $1 + S_\infty^2$ from the case of upright convection⁵.

433 The significance of this will be discussed further below.

434 First however, it is useful to note that another potential mechanism by which SI/CI could modify
435 Ekman adjustment is through the convergence of along-front momentum near the lower bound-
436 ary associated with the SI/CI overturning cells (see for example figure 3). This convergence of
437 momentum could in principle act to accelerate ageostrophic along-slope flows near the boundary,
438 which would help to maintain an along-slope bottom stress, countering the Ekman arrest process.

439 However, investigation of the numerical simulations we performed suggest this mechanism is not
440 active. Instead, the principal balance in the along-slope momentum budget (8) is between the flux
441 convergence terms and the Coriolis acceleration, ie. the momentum flux convergence drives a sec-
442 ondary circulation in the cross-slope direction rather than accelerating an along-slope flow (figure
443 8, consistent with the surface boundary layer results of TF10).

444 This suggests that the Ekman buoyancy arrest process persists even in the presence of finite
445 amplitude SI/CI. The timescale for the buoyancy arrest process is,

$$T_{E-SI/CI} = \frac{V_\infty^2 (1 + S_\infty^2)^2}{2 N_\infty S_\infty^3 u_o^{*2}}, \quad (50)$$

446 where $u_o^* = \sqrt{\tau_o / \rho_o}$ is the initial friction velocity, before Ekman adjustment has begun. This
447 timescale follows directly from the derivation given in Brink and Lentz (2010, their equation 26),
448 using a value of the critical Richardson number of $Ri_c = 1 + S_\infty^2$ which, for flow in approximate
449 geostrophic balance, gives $q = 0$ (Allen and Newberger 1998). The ability of this timescale to col-

⁵The relaminarization height (Ruan et al. 2019) of the boundary layer, which marks the point at which turbulence in the boundary layer is suppressed by viscous effects, will similarly be increased by a factor of $1 + S_\infty^2$ by SI/CI. This can be seen by replacing the approximate stress relation in Ruan et al. (2019, their equation 13) with $\tau^y / \rho_o \approx C_d [V_\infty - H N_\infty^2 \theta / f(1 + S_\infty^2)]^2$ to reflect the reduced geostrophic shear.

450 lapse the various numerical model results is striking (figure 16). The SI/CI arrest process timescale
 451 can also be compared to that for classic Ekman arrest where the boundary layer is assumed to be
 452 well-mixed (ie. $Ri_c = 0$), such that,

$$T_E = \frac{V_\infty^2(1+S_\infty^2)}{2N_\infty S_\infty^3 u_o^{*2}}. \quad (51)$$

453 SI/CI thus extends the arrest process by a factor of $1 + S_\infty^2$ via restratification of the boundary layer,
 454 which reduces the strength of the thermal wind shear.

455 A detailed analysis of the energetics of Ekman adjustment of the BBL in the presence of SI/CI
 456 will be the subject of a future manuscript, however it is worth briefly noting the effect that these
 457 processes may have on the energetics of the general ocean circulation, where bottom drag over
 458 topography is believed to be a key sink of kinetic energy from the balanced flow field (Ferrari and
 459 Wunsch 2009; Sen et al. 2008; Arbic et al. 2009). The combined energy loss from the geostrophic
 460 flow due to bottom drag and the vertically integrated SI/CI dissipation can be conceptualized as an
 461 effective dissipation (cf. Thomas and Taylor 2010),

$$DISS_{EFF} = -\tau^y v_g|_{z=0} - \rho_o \int_0^\infty \varepsilon_{SI} dz, \quad (52)$$

462 which, using (48), and the definition of the change in geostrophic velocity across the boundary
 463 layer, $\Delta v_g = H N_\infty^2 \theta / f(1 + S_\infty^2)$, can be written as,

$$DISS_{EFF} = -\tau^y \left(v_g|_{z=0} + \frac{1}{2} \Delta v_g \right). \quad (53)$$

464 Considering the development of thermal wind shear during the Ekman arrest process, which re-
 465 duces the bottom geostrophic velocity from the interior values such that $v_g|_{z=0} = V_\infty - \Delta v_g$, the
 466 effective dissipation can also be written as, $DISS_{EFF} = -\tau^y (V_\infty - \Delta v_g / 2)$. Thus, while the Ekman
 467 arrest process reduces the energy lost to bottom drag on the geostrophic flow through the devel-
 468 opment of thermal wind shear, the presence of SI/CI offsets half of this reduction directly through

⁴⁶⁹ enhanced dissipation of kinetic energy extracted from the geostrophic flow either directly through
⁴⁷⁰ GSP_s or indirectly through the release of available potential energy (which in the Ekman arrest
⁴⁷¹ process is ultimately sourced from the mean kinetic energy, Umlauf et al. 2015).

⁴⁷² **6. Summary and Discussion**

⁴⁷³ Recently there has been a renewed interest in the dynamics of the BBL, motivated in part by the
⁴⁷⁴ possibility that recent advances in understanding submesoscale processes at the ocean's surface
⁴⁷⁵ might also provide insight into the physical processes at the bottom (McWilliams 2016; Wenegrat
⁴⁷⁶ et al. 2018). In this manuscript we focused on the case of an interior flow along isobaths of a
⁴⁷⁷ sloping lower boundary which generates a downslope Ekman transport, as a BBL counterpart to
⁴⁷⁸ the well-studied case of downfront surface wind stress. We show that there exists a state of forced
⁴⁷⁹ centrifugal and symmetric instability in the BBL, which behaves much like the state of forced
⁴⁸⁰ symmetric instability in the surface boundary layer (TF10; Thomas and Taylor 2010). Importantly,
⁴⁸¹ the fact that the BBL evolves to reach the state of marginal stability to SI/CI (ie. $q \approx 0$) provides
⁴⁸² a strong constraint on the evolution, with major consequences including:

- ⁴⁸³ 1. The slope Ekman buoyancy flux, EBF_s (23), controls both the rate of change of buoyancy
⁴⁸⁴ in the boundary layer (22), and the slope-normal flux of PV (19). This allows the governing
⁴⁸⁵ equation for the height of the low PV layer to be expressed as a simple ordinary differential
⁴⁸⁶ equation involving the bottom stress, slope angle, and Coriolis frequency (27).

- ⁴⁸⁷ 2. SI/CI restratifies the BBL, such that the approximate stratification of the boundary layer goes
⁴⁸⁸ as $N_\infty^2 S_\infty^2 / (1 + S_\infty^2)$ (Allen and Newberger 1998). Thus, the BBL may retain significant strati-
⁴⁸⁹ fication, particularly in regimes with large interior slope Burger numbers. This finding should
⁴⁹⁰ be considered when interpreting observations, as our results suggest significant turbulent dis-

491 sipation via SI/CI is possible even in stratified regions that would not necessarily be easily
492 identifiable as a boundary layer in terms of the buoyancy profile alone. For example in ob-
493 servations of SI/CI unstable conditions in the deep Orkney Passage (Naveira Garabato et al.
494 2019) interior slope Burger numbers of $S_\infty \approx 1.4$ suggest that SI/CI may be active in regions
495 where the stratification is as large as 2/3 of the interior values.

496 3. Downslope Ekman transport always tends to generate conditions unstable to SI/CI through
497 the destruction of boundary layer PV. However, it is also necessary to consider the ratio
498 of the slope Monin-Obukhov length, L_s (34), to the boundary layer depth when evaluating
499 whether SI/CI will be present — specifically when L_s/H is large the boundary layer remains
500 unstratified and SI/CI is absent. We note however that in the case that L_s/H is large because
501 S_∞ is small, baroclinic instabilities are likely to emerge rapidly (though not present in the 2D
502 simulations used here; Brink and Cherian 2013; Wenegrat et al. 2018).

503 4. The primary energy source for SI/CI in the BBL is the slope Geostrophic Shear Produc-
504 tion, GSP_s (39), whereby slope-normal eddy fluxes extract energy from the background
505 geostrophic shear. The energy source for the BBL instabilities can therefore involve mixed
506 SI/CI modes with energy extracted from the geostrophic flow through both lateral and vertical
507 shear production terms (40). The slope Burger number provides an indicator of whether the
508 instability will be of the centrifugal ($S_\infty > 1$) or symmetric ($S_\infty < 1$) type, (41) and (42).

509 5. The dissipation rate in the boundary layer due to SI/CI scales with the EBF_s , and decreases
510 linearly through the boundary layer height (48), hence the integrated SI/CI dissipation goes
511 as $(H/2)EBF_s$. In the surface boundary layer similar results (eg. Thomas and Taylor 2010)
512 have been used as the basis for parameterization for models that do not directly resolve SI

513 (Bachman et al. 2017), and our results suggest a similar parameterization is possible for the
514 BBL.

515 6. SI/CI extends the Ekman arrest time by a factor of $(1 + S_\infty^2)$, and increases the arrested Ekman
516 height by the same factor, but does not stop the buoyancy arrest process. The total loss of
517 energy from the balanced flow through bottom drag and SI/CI during Ekman arrest can be
518 conceptualized as an effective dissipation (53), which shows that energy extraction from the
519 geostrophic shear by SI/CI offsets exactly half of the reduction in bottom drag due to the
520 development of thermal wind shear in the boundary layer. SI/CI also increases the time-
521 integrated dissipation by slowing the Ekman arrest process, ie. slowing the decay of the
522 bottom stress.

523 Beyond instabilities of the BBL itself, a variety of recent work has also noted that the formation
524 of topographic wakes, characterized by the shedding of BBL fluid with $f q < 0$, appears to be a
525 common feature in realistic submesoscale-resolving simulations (Molemaker et al. 2015; Dewar
526 et al. 2015; Gula et al. 2016; Srinivasan et al. 2019). These topographic wakes appear to be par-
527 ticularly susceptible to CI, which generate dissipation rates that may be sufficiently large to affect
528 the energetics of regional or even global ocean circulation (Gula et al. 2016). The development
529 of these wake instabilities will be sensitive to the upstream BBL evolution, and hence they may
530 also be influenced by SI/CI in the BBL. For instance, when BBL instabilities are able to bring the
531 boundary layer to the state of $q \approx 0$ before boundary layer separation, the subsequent topographic
532 wake can be stabilized to further instabilities. A manuscript detailing how the instabilities and en-
533 ergetics of topographic wakes depends on the upstream BBL evolution is currently in preparation.

534 One additional aspect of how BBL instabilities can modulate flow-topography interaction —
535 which was not a specific focus of the work presented here — is by affecting the irreversible mixing

536 of buoyancy along topography. This topic has broad implications for the large-scale ocean circu-
537 lation, and, for example, recent observational and numerical modeling work has suggested that
538 submesoscale instabilities along topography may play an important role in the deep-overturning
539 circulation (Ruan et al. 2017; Wenegrat et al. 2018; Callies 2018; Naveira Garabato et al. 2019).
540 The distinction between SI and CI modes, which we argued above was somewhat artificial in re-
541 gards to the kinetic energy budget, may be of more significance when considering the mixing of
542 buoyancy. Specifically, simulations of interior CI suggest very high mixing efficiencies (Jiao and
543 Dewar 2015), in contrast to the SI modes which are aligned primarily along isopycnals and hence
544 tend to have very low mixing efficiencies. Further investigation of SI/CI in the BBL and topo-
545 graphic wakes will help clarify the role of submesoscale instabilities in watermass transformation
546 along topography.

547 *Acknowledgments.* J.O.W. thanks Bertrand Delorme, John Taylor, and Andrew Thompson for
548 stimulating discussions during the preparation of this manuscript. The comments of two anonym-
549 ous reviewers are also gratefully acknowledged. Funding for this work was provided by NSF
550 grant OCE-1756118. All numerical simulation output used in this manuscript was created us-
551 ing the open source software Dedalus, which is available for download from [http://dedalus-](http://dedalus-project.org/)
552 [project.org/](http://dedalus-project.org/).

553 APPENDIX

554 In this appendix we derive the approximate cross-slope transport equation, (21). This follows
555 closely from Brink and Lentz (2010), however we integrate over a finite depth, and retain entrain-
556 ment fluxes of buoyancy. First, taking the time-derivative of (7), and combining with (8), gives a

single expression that combines the horizontal momentum equations,

$$\frac{\partial^2 \langle u \rangle}{\partial t^2} + f^2 \langle u \rangle = f \frac{\partial F^y}{\partial z} + \frac{\partial^2 F^x}{\partial z \partial t} + \frac{\partial \langle b \rangle}{\partial t} \theta, \quad (\text{A1})$$

where $F^x = -\langle u'w' \rangle + v \partial \langle u \rangle / \partial z$ is the combined turbulent and diffusive slope-normal flux of across-slope momentum, and F^y is defined similarly for the along-slope momentum.

Variables in this equation can be scaled as $u \sim U$, $t \sim T$, $z \sim H$, $F^y \sim \tau^y / \rho_o$, $F^x \sim \tau^x / \rho_o$, and $b \sim TUN_\infty^2 \theta$. This scaling for the buoyancy is a consequence of the assumption that in the regimes of interest here the across-slope advection of buoyancy is leading-order in the mean buoyancy equation (10). Using these scalings, the ratio of the first term on the left hand side to the Coriolis acceleration is

$$\frac{U}{T^2 f^2 U} \sim O(T^2 f^2)^{-1}. \quad (\text{A2})$$

The ratio of the second term on the right-hand side to the first term on the right-hand side is,

$$\frac{\tau^x H}{HTf\tau^y} \leq O(Tf)^{-1}, \quad (\text{A3})$$

where we have assumed that $\tau^x \leq \tau^y$ as the interior velocity is aligned in the y-direction. Thus, both the first term on the left-hand side, and the second-term on the right hand side can be neglected when considering subinertial motions where $Tf \gg 1$. In contrast, the last term on the right-hand side, involving the perturbation buoyancy, scales relative to the Coriolis acceleration as,

$$\frac{TUN_\infty^2 \theta^2}{Tf^2 U} \sim S_\infty^2, \quad (\text{A4})$$

which is not necessarily small (table 1). We thus neglect time-dependence of the across-slope momentum and stress, while retaining the influence of buoyancy on the across-slope momentum equation, as in Brink and Lentz (2010), such that

$$f^2 \langle u \rangle \simeq f \frac{\partial F^y}{\partial z} + \frac{\partial \langle b \rangle}{\partial t} \theta. \quad (\text{A5})$$

573 Now, integrate over a layer of thickness z' , using the mean buoyancy equation (10) to replace
 574 the rate of change of buoyancy,

$$f^2 (1 + S_\infty^2) \int_0^{z'} \langle u \rangle dz \simeq f F^y|_{z=z'} - f \frac{\langle \tau^y \rangle}{\rho_o} - \theta \langle w' b' \rangle|_{z=z'} + \theta \kappa \frac{\partial \langle b \rangle}{\partial z}|_{z=z'} + \theta \kappa N_\infty^2. \quad (\text{A6})$$

575 The final two terms in this equation involve diffusive buoyancy fluxes, and both can be scaled
 576 relative to the bottom stress as

$$\frac{\kappa N_\infty^2 \theta \rho_o}{f \tau^y} = \frac{\kappa \rho_o f}{\theta \tau^y} S_\infty^2 < \frac{\kappa \rho_o f}{\theta \tau^y} (1 + S_\infty^2), \quad (\text{A7})$$

577 ie. the ratio of the Thorpe transport (Thorpe 1987), κ/θ , to the Ekman transport, $\tau^y/\rho_o f(1 + S_\infty^2)$.

578 This ratio is generally very small, hence we neglect the diffusive flux of buoyancy throughout,
 579 however if desired it is straightforward to incorporate viscous/diffusive fluxes into the theory de-
 580 veloped here. We also note that this assumption is sometimes violated in the late-time evolution
 581 of simulations with large S_∞ , which undergo significant Ekman arrest (section 5). Hence for the
 582 purposes of comparison between the numerical simulations and theory in section 3c we exclude
 583 instances where $EBF_s/\kappa N_\infty^2 < 3$ for consistency with (A7), although our results are not sensitive
 584 to the particular cutoff value used. Similar arguments also allow for ignoring the diffusive flux
 585 of momentum at z' . In contrast the resolved turbulent buoyancy and momentum fluxes scale with
 586 the EBF_s and bottom stress, and are therefore not necessarily small, depending on where in the
 587 boundary layer z' is taken to be.

588 Thus, an approximate form for the depth integrated cross-slope transport equation is,

$$f^2 (1 + S_\infty^2) \int_0^{z'} u dz \simeq -f \langle v' w' \rangle|_{z=z'} - f \frac{\langle \tau^y \rangle}{\rho_o} - \theta \langle w' b' \rangle|_{z=z'}. \quad (\text{A8})$$

589 Finally, we further note that by dividing (A5) by f , and subtracting the result from (8) it can be
 590 seen that the above scaling arguments also imply $\partial \langle v \rangle / \partial t \simeq -f^{-1} \theta \partial \langle b \rangle / \partial t$. An alternate deriva-
 591 tion of this relationship involves directly scaling the across-slope momentum equation, which

592 indicates that at subinertial timescales the flow is in approximate geostrophic balance outside the
593 near-boundary Ekman layer, ie. $-f\langle v \rangle \simeq \langle b \rangle \theta$ (see for example figure 8), which can then be
594 differentiated in time. Thus, in the BBL setup considered here — where the mean geostrophic
595 velocity evolves in time — the rate of change of along-slope velocity in the PV flux equation (18)
596 is not necessarily negligible, unlike in the frontal-zone configuration considered in (TF10) where
597 the mean geostrophic velocity did not evolve in time.

598 References

- 599 Allen, J. S., and P. A. Newberger, 1993: Downwelling Circulation on the Oregon Continental
600 Shelf. Part I: Response to Idealized Forcing. *Journal of Physical Oceanography*, **26**, 2011–
601 2035, doi:10.1175/1520-0485(1996)026<2011:DCOTOC>2.0.CO;2.
- 602 Allen, J. S., and P. A. Newberger, 1998: On Symmetric Instabilities in Oceanic Bottom Boundary
603 Layers. *Journal of Physical Oceanography*, **28** (6), 1131–1151, doi:10.1175/1520-0485(1998)
604 028<1131:OSIIOB>2.0.CO;2, URL <http://journals.ametsoc.org/doi/abs/10.1175/1520-0485%281998%29028%3C1131%3AOSIIOB%3E2.0.CO%3B2>.
- 605 Arbic, B. K., and Coauthors, 2009: Estimates of bottom flows and bottom boundary layer dissipation
606 of the oceanic general circulation from global high-resolution models. *Journal of Geophysical Research*, **114** (C2), C02 024, doi:10.1029/2008JC005072, URL <http://doi.wiley.com/10.1029/2008JC005072>.
- 607 Bachman, S., B. Fox-Kemper, J. Taylor, and L. Thomas, 2017: Parameterization of Frontal Symmetric
608 Instabilities. I: Theory for Resolved Fronts. *Ocean Modelling*, **109**, 72–95, doi:10.1016/j.ocemod.2016.12.003, URL <http://linkinghub.elsevier.com/retrieve/pii/S1463500316301482>.

- 613 Benthuysen, J., and L. N. Thomas, 2012: Friction and Diapycnal Mixing at a Slope: Boundary
614 Control of Potential Vorticity. *Journal of Physical Oceanography*, **42** (9), 1509–1523, doi:10.
615 1175/JPO-D-11-0130.1, URL <http://journals.ametsoc.org/doi/abs/10.1175/JPO-D-11-0130.1>.
- 616 Brink, K. H., and D. A. Cherian, 2013: Instability of an idealized tidal mixing front: Sym-
617 metric instabilities and frictional effects. *Journal of Marine Research*, **71** (6), 425–450, doi:
618 10.1357/002224013812587582, URL <http://openurl.ingenta.com/content/xref?genre=article&issn=0022-2402&volume=71&issue=6&spage=425>.
- 620 Brink, K. H., and S. J. Lentz, 2010: Buoyancy Arrest and Bottom Ekman Transport. Part I: Steady
621 Flow. *Journal of Physical Oceanography*, **40** (4), 621–635, doi:10.1175/2009JPO4266.1, URL
622 <http://journals.ametsoc.org/doi/abs/10.1175/2009JPO4266.1>.
- 623 Burns, K. J., G. M. Vasil, J. S. Oishi, D. Lecoanet, and B. P. Brown, 2019: Dedalus: A Flexible
624 Framework for Numerical Simulations with Spectral Methods. *arXiv:1905.10388 [astro-ph, physics:physics]*, URL <http://arxiv.org/abs/1905.10388>, arXiv: 1905.10388.
- 626 Callies, J., 2018: Restratification of Abyssal Mixing Layers by Submesoscale Baroclinic Eddies.
627 *Journal of Physical Oceanography*, **48** (9), 1995–2010, doi:10.1175/JPO-D-18-0082.1, URL
628 <http://journals.ametsoc.org/doi/10.1175/JPO-D-18-0082.1>.
- 629 D’Asaro, E., C. Lee, L. Rainville, R. Harcourt, and L. Thomas, 2011: Enhanced Turbulence
630 and Energy Dissipation at Ocean Fronts. *Science*, **332** (6027), 318–322, doi:10.1126/science.1201515, URL <http://www.sciencemag.org/cgi/doi/10.1126/science.1201515>.
- 632 Deardorff, J. W., G. E. Willis, and D. K. Lilly, 1969: Laboratory investigation
633 of non-steady penetrative convection. *Journal of Fluid Mechanics*, **35** (1), 7–31,

634 doi:10.1017/S0022112069000942, URL [https://www.cambridge.org/core/product/identifier/
635 S0022112069000942/type/journal_article](https://www.cambridge.org/core/product/identifier/S0022112069000942/type/journal_article).

636 Dewar, W. K., J. C. McWilliams, and M. J. Molemaker, 2015: Centrifugal Instability and Mixing
637 in the California Undercurrent. *Journal of Physical Oceanography*, **45** (5), 1224–1241, doi:
638 10.1175/JPO-D-13-0269.1, URL <http://journals.ametsoc.org/doi/10.1175/JPO-D-13-0269.1>.

639 Ferrari, R., and C. Wunsch, 2009: Ocean Circulation Kinetic Energy: Reservoirs, Sources,
640 and Sinks. *Annual Review of Fluid Mechanics*, **41** (1), 253–282, doi:10.1146/annurev.fluid.
641 40.111406.102139, URL <http://www.annualreviews.org/doi/10.1146/annurev.fluid.40.111406.102139>.
642

643 Garrett, C., P. MacCready, and P. Rhines, 1993: Boundary Mixing and Arrested Ekman Lay-
644 ers: Rotating Stratified Flow Near a Sloping Boundary. *Annual Review of Fluid Mechanics*,
645 **25** (1), 291–323, doi:10.1146/annurev.fl.25.010193.001451, URL <http://www.annualreviews.org/doi/10.1146/annurev.fl.25.010193.001451>.
646

647 Grisouard, N., 2018: Extraction of Potential Energy from Geostrophic Fronts by Iner-
648 tial–Symmetric Instabilities. *Journal of Physical Oceanography*, **48** (5), 1033–1051, doi:
649 10.1175/JPO-D-17-0160.1, URL <http://journals.ametsoc.org/doi/10.1175/JPO-D-17-0160.1>.

650 Gula, J., M. J. Molemaker, and J. C. McWilliams, 2016: Topographic generation of submesoscale
651 centrifugal instability and energy dissipation. *Nature Communications*, **7**, 12811, doi:10.1038/ncomms12811,
652 URL <http://www.nature.com/doifinder/10.1038/ncomms12811>.

653 Haine, T. W. N., and J. Marshall, 1998: Gravitational, Symmetric, and Baroclinic Instabil-
654 ity of the Ocean Mixed Layer. *Journal of Physical Oceanography*, **28** (4), 634–658, doi:

- 655 10.1175/1520-0485(1998)028<0634:GSABIO>2.0.CO;2, URL <http://journals.ametsoc.org/doi/abs/10.1175/1520-0485%281998%29028%3C0634%3AGSABIO%3E2.0.CO%3B2>.
- 656
- 657 Jiao, Y., and W. K. Dewar, 2015: The Energetics of Centrifugal Instability. *Journal of Phys-*
658 *ical Oceanography*, **45** (6), 1554–1573, doi:10.1175/JPO-D-14-0064.1, URL <http://journals.ametsoc.org/doi/10.1175/JPO-D-14-0064.1>.
- 659
- 660 MacCready, P., and P. B. Rhines, 1991: Buoyant inhibition of Ekman transport on a slope
661 and its effect on stratified spin-up. *Journal of Fluid Mechanics*, **223** (-1), 631, doi:10.1017/S0022112091001581, URL http://www.journals.cambridge.org/abstract_S0022112091001581.
- 662
- 663 MacCready, P., and P. B. Rhines, 1993: Slippery Bottom Boundary Layers on a Slope.
664 *Journal of Physical Oceanography*, **23** (1), 5–22, doi:10.1175/1520-0485(1993)023<0005:SBBLOA>2.0.CO;2, URL <http://journals.ametsoc.org/doi/abs/10.1175/1520-0485%281993%29023%3C0005%3ASBBLOA%3E2.0.CO%3B2>.
- 665
- 666
- 667 McWilliams, J. C., 2016: Submesoscale currents in the ocean. *Proceedings of the Royal Society A: Mathematical, Physical and Engineering Science*, **472** (2189), 20160117, doi:10.1098/rspa.
668 2016.0117, URL <http://rspa.royalsocietypublishing.org/lookup/doi/10.1098/rspa.2016.0117>.
- 669
- 670 Molemaker, M. J., J. C. McWilliams, and W. K. Dewar, 2015: Submesoscale Instability and
671 Generation of Mesoscale Anticyclones near a Separation of the California Undercurrent. *Jour-*
672 *nal of Physical Oceanography*, **45** (3), 613–629, doi:10.1175/JPO-D-13-0225.1, URL <http://journals.ametsoc.org/doi/abs/10.1175/JPO-D-13-0225.1>.
- 673
- 674 Naveira Garabato, A. C., and Coauthors, 2019: Rapid mixing and exchange of deep-ocean waters
675 in an abyssal boundary current. *Proceedings of the National Academy of Sciences*, **116** (27),

- 676 13 233–13 238, doi:10.1073/pnas.1904087116, URL <http://www.pnas.org/lookup/doi/10.1073/pnas.1904087116>.
- 677
- 678 Ruan, X., A. F. Thompson, M. M. Flexas, and J. Sprintall, 2017: Contribution of topographically
679 generated submesoscale turbulence to Southern Ocean overturning. *Nature Geoscience*, **10** (11),
680 840–845, doi:10.1038/ngeo3053, URL <http://www.nature.com/doifinder/10.1038/ngeo3053>.
- 681
- 682 Ruan, X., A. F. Thompson, and J. R. Taylor, 2019: The Evolution and Arrest of a Turbulent Stratified
683 Oceanic Bottom Boundary Layer over a Slope: Downslope Regime. *Journal of Physical
684 Oceanography*, **49** (2), 469–487, doi:10.1175/JPO-D-18-0079.1, URL <http://journals.ametsoc.org/doi/10.1175/JPO-D-18-0079.1>.
- 685
- 686 Sen, A., R. B. Scott, and B. K. Arbic, 2008: Global energy dissipation rate of deep-ocean low-
687 frequency flows by quadratic bottom boundary layer drag: Computations from current-meter
688 data. *Geophysical Research Letters*, **35** (9), L09 606, doi:10.1029/2008GL033407, URL <http://doi.wiley.com/10.1029/2008GL033407>.
- 689
- 690 Srinivasan, K., J. C. McWilliams, M. J. Molemaker, and R. Barkan, 2019: Submesoscale Vortical
691 Wakes in the Lee of Topography. *Journal of Physical Oceanography*, **49** (7), 1949–1971, doi:
692 10.1175/JPO-D-18-0042.1, URL <http://journals.ametsoc.org/doi/10.1175/JPO-D-18-0042.1>.
- 693
- 694 Stone, P. H., 1966: On Non-Geostrophic Baroclinic Stability. *Journal of the Atmospheric Sciences*, **23** (4), 390–400, doi:10.1175/1520-0469(1966)023<0390:ONGBS>2.0.CO;
695 2, URL <http://journals.ametsoc.org/doi/abs/10.1175/1520-0469%281966%29023%3C0390%3AONGBS%3E2.0.CO%3B2>.
- 696
- 697 Taylor, J. R., and R. Ferrari, 2009: On the equilibration of a symmetrically unstable front via a secondary shear instability. *Journal of Fluid Mechanics*, **622**, 103, doi:10.1017/

- 698 S0022112008005272, URL http://www.journals.cambridge.org/abstract_S0022112008005272.
- 699 Taylor, J. R., and R. Ferrari, 2010: Buoyancy and Wind-Driven Convection at Mixed Layer Den-
- 700 sity Fronts. *Journal of Physical Oceanography*, **40** (6), 1222–1242, doi:10.1175/2010JPO4365.
- 701 1, URL <http://journals.ametsoc.org/doi/abs/10.1175/2010JPO4365.1>.
- 702 Thomas, L., and R. Ferrari, 2008: Friction, Frontogenesis, and the Stratification of the Sur-
- 703 face Mixed Layer. *Journal of Physical Oceanography*, **38** (11), 2501–2518, doi:10.1175/
- 704 2008JPO3797.1, URL <http://journals.ametsoc.org/doi/abs/10.1175/2008JPO3797.1>.
- 705 Thomas, L. N., 2005: Destruction of Potential Vorticity by Winds. *Journal of Physical Oceanog-*
- 706 *rphy*, **35** (12), 2457–2466, doi:10.1175/JPO2830.1, URL <http://journals.ametsoc.org/doi/abs/10.1175/JPO2830.1>.
- 707
- 708 Thomas, L. N., 2008: Formation of intrathermocline eddies at ocean fronts by wind-driven
- 709 destruction of potential vorticity. *Dynamics of Atmospheres and Oceans*, **45** (3-4), 252–
- 710 273, doi:10.1016/j.dynatmoce.2008.02.002, URL <https://linkinghub.elsevier.com/retrieve/pii/S0377026508000353>.
- 711
- 712 Thomas, L. N., and J. R. Taylor, 2010: Reduction of the usable wind-work on the general cir-
- 713 culation by forced symmetric instability. *Geophysical Research Letters*, **37** (18), n/a–n/a, doi:
- 714 10.1029/2010GL044680, URL <http://doi.wiley.com/10.1029/2010GL044680>.
- 715
- 716 Thomas, L. N., J. R. Taylor, E. A. D'Asaro, C. M. Lee, J. M. Klymak, and A. Shcherbina, 2016:
- 717 Symmetric Instability, Inertial Oscillations, and Turbulence at the Gulf Stream Front. *Journal of*
- 718 *Physical Oceanography*, **46** (1), 197–217, doi:10.1175/JPO-D-15-0008.1, URL <http://journals.ametsoc.org/doi/10.1175/JPO-D-15-0008.1>.

- 719 Thomas, L. N., J. R. Taylor, R. Ferrari, and T. M. Joyce, 2013: Symmetric instability in the Gulf
720 Stream. *Deep Sea Research Part II: Topical Studies in Oceanography*, **91**, 96–110, doi:10.1016/j.dsr2.2013.02.025, URL <http://linkinghub.elsevier.com/retrieve/pii/S0967064513000829>.
- 721
- 722 Thorpe, S. A., 1987: Current and Temperature Variability on the Continental Slope. *Philosophical
723 Transactions of the Royal Society of London. Series A, Mathematical and Physical Sciences*,
724 **323 (1574)**, 471–517, URL <http://www.jstor.org/stable/38149>.
- 725 Umlauf, L., W. D. Smyth, and J. N. Moum, 2015: Energetics of Bottom Ekman Layers dur-
726 ing Buoyancy Arrest. *Journal of Physical Oceanography*, **45 (12)**, 3099–3117, doi:10.1175/
727 JPO-D-15-0041.1, URL <http://journals.ametsoc.org/doi/10.1175/JPO-D-15-0041.1>.
- 728 Wenegrat, J. O., J. Callies, and L. N. Thomas, 2018: Submesoscale Baroclinic Instability in the
729 Bottom Boundary Layer. *Journal of Physical Oceanography*, **48 (11)**, 2571–2592, doi:10.1175/
730 JPO-D-17-0264.1, URL <http://journals.ametsoc.org/doi/10.1175/JPO-D-17-0264.1>.
- 731 Wenegrat, J. O., and M. J. McPhaden, 2016: Wind, Waves, and Fronts: Frictional Effects in a
732 Generalized Ekman Model. *Journal of Physical Oceanography*, **46 (2)**, 371–394, doi:10.1175/
733 JPO-D-15-0162.1, URL <http://journals.ametsoc.org/doi/abs/10.1175/JPO-D-15-0162.1>.
- 734 Yankovsky, E., and S. Legg, 2019: Symmetric and Baroclinic Instability in Dense Shelf Overflows.
735 *Journal of Physical Oceanography*, **49 (1)**, 39–61, doi:10.1175/JPO-D-18-0072.1, URL <http://journals.ametsoc.org/doi/10.1175/JPO-D-18-0072.1>.
- 736

737 **LIST OF TABLES**

738 **Table 1.** Summary of numerical simulations. All simulations are run with $f = 10^{-4}$
739 s^{-1} , and an interior velocity of $V_\infty = 0.1 \text{ m s}^{-1}$ except as indicated by a \ddagger
740 where an increased velocity of $V_\infty = 0.2 \text{ m s}^{-1}$ was used. Simulations that were
741 dominated by convective instability are indicated by the \dagger symbol (section 3c). . . . 39

742 TABLE 1. Summary of numerical simulations. All simulations are run with $f = 10^{-4}$ s $^{-1}$, and an interior
 743 velocity of $V_\infty = 0.1$ m s $^{-1}$ except as indicated by a \ddagger where an increased velocity of $V_\infty = 0.2$ m s $^{-1}$ was used.
 744 Simulations that were dominated by convective instability are indicated by the \dagger symbol (section 3c).

Name	Interior Stratification N_∞^2 (s $^{-2}$)	Slope Angle θ	Slope Burger Number $S_\infty = N_\infty \tan \theta / f$	Model Configuration
				$L_x \times L_z$ – Run duration
CI-1	10^{-5}	0.1	3.2	1 km x 200 m – 40 days
	10^{-5}	0.05	1.6	1 km x 200 m – 40 days
	10^{-6}	0.1	1	1 km x 300 m – 30 days
SI-1	10^{-5}	0.02	0.6	1 km x 200 m – 40 days
\ddagger	10^{-5}	0.02	0.6	2 km x 300 m – 15 days
	10^{-6}	0.06	0.6	1 km x 200 m – 15 days
	5×10^{-6}	0.02	0.45	1 km x 200 m – 40 days
\dagger	10^{-6}	0.01	0.1	1 km x 200 m – 40 days
\dagger	10^{-7}	0.02	0.06	1 km x 200 m – 40 days
CONV-1 \dagger	10^{-7}	0.005	0.02	1 km x 200 m – 40 days

745 LIST OF FIGURES

- Fig. 1.** Schematic of the numerical model domain (panel A), with initial condition consisting of a uniformly stratified interior (with buoyancy contours indicated by thin black lines) and barotropic interior flow over a sloping lower boundary. An example of the adjustment of the boundary layer towards thermal wind balance is shown in panel B, where downslope Ekman transport generates thermal wind shear in the bottom boundary layer, reducing the near-bottom velocities. The rotated coordinate system is also shown, with standard non-rotated coordinates denoted using the hat notation.

Fig. 2. Overview of the evolution of simulation SI-1 (with parameters as given in table 1). From top to bottom the panels give the across-slope velocity (u), the total along-slope velocity ($v_T = v + V_\infty$), the vertical buoyancy gradient (N^2), and the PV (q). All values are averaged in the across-slope (x) direction, and normalized as indicated in each plot. The evolution of the low PV layer depth H , as predicted by (27), is shown in the bottom panel in black.

Fig. 3. Snapshot of the across-slope velocity field (u , color scale) from day 12 of run SI-1. The banded velocity structure is typical of symmetric instability, where the fastest growing mode is oriented along isopycnals (black contours). The height of the low PV layer (H , section 3b) and the convective layer (h , section 3c) as determined from the numerical solutions are indicated along the right ordinate by the large and small triangles, respectively.

Fig. 4. Cross-frontal section detailing the spatial distribution of the fastest growing instability type predicted from linear theory for run SI-1 on day 12 (as in figure 3). Parameter space is divided into mixed centrifugal-symmetric (CI-SI), symmetric (SI), gravitational (GRAV), and mixed gravitational-symmetric (GRAV-SI) following the balanced Richardson number criteria laid out in Thomas et al. (2013, as discussed in section 2b). Isopycnals are shown with black contours. All fields are averaged over a 4 hour period, and the height of the low PV layer (H , section 3b) and the convective layer (h , section 3c) as determined from the numerical solutions are indicated along the right ordinate by the large and small triangles, respectively.

Fig. 5. As in figure 2, but for simulation CI-1 (with parameters as given in table 1). From top to bottom the panels give the across-slope velocity (u , note the reduced color scale from figure 2), the total along-slope velocity ($v_T = v + V_\infty$), the vertical buoyancy gradient (N^2), and the PV (q). All values are averaged in the across-slope (x) direction, and normalized as indicated in each plot. The evolution of the low PV layer depth H , as predicted by (27), is shown in the bottom panel in black.

Fig. 6. As in figure 3, but for run CI-1 on day 12.

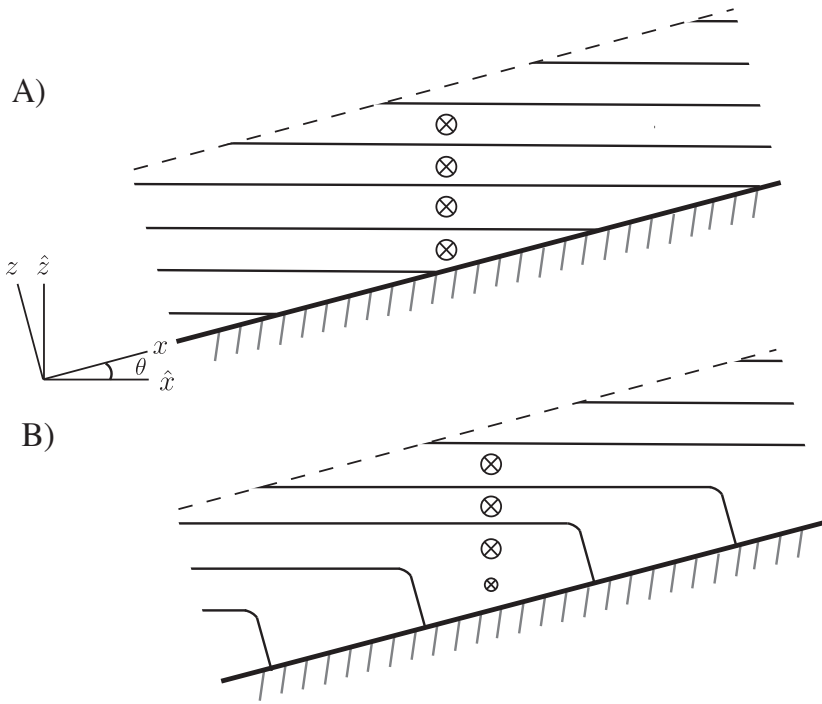
Fig. 7. Cross-frontal section detailing the spatial distribution of the fastest growing instability type predicted from linear theory for run CI-1 on day 12 (as in figure 6). See the caption of figure 4 for definitions.

Fig. 8. Dominant terms in the momentum equations for simulation SI-1, averaged in the across-slope direction (x) and over days 11-13. The across-slope momentum budget, (7), is largely in a geostrophic balance between buoyancy perturbations and Coriolis accelerations, with some additional contribution from the turbulent momentum flux divergence (left panel). The along-slope momentum budget, (8), is in approximate Ekman balance, with Coriolis accelerations balancing the turbulent momentum flux divergence (right panel). The height of the low PV layer (H , large triangle) and the convective layer (h , small triangle) are indicated along the right ordinate in each plot.

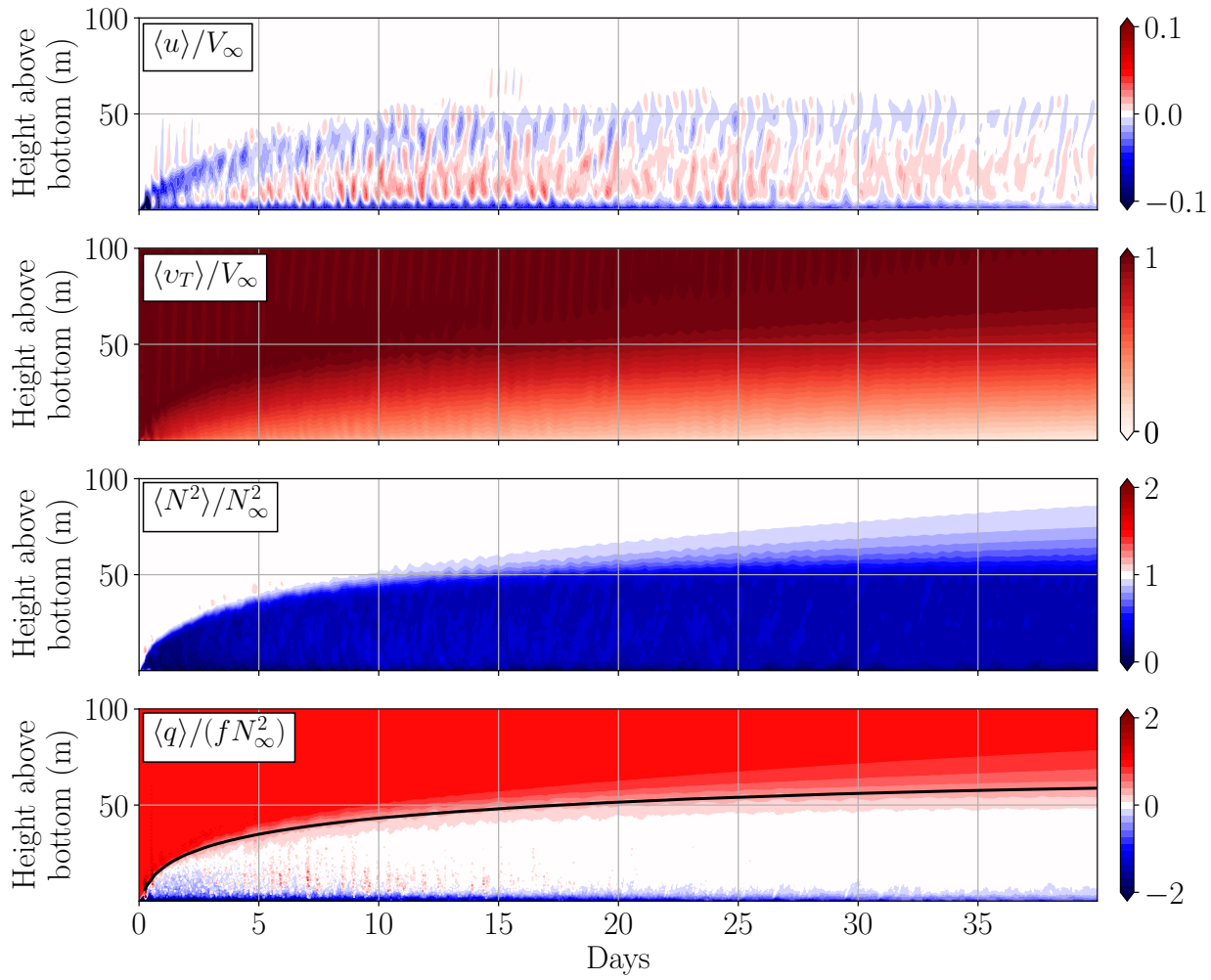
- 790 **Fig. 9.** Terms from the slope-normal PV flux equation, (19), averaged horizontally (x) and over
 791 days 11-13 for simulation SI-1. A) Away from the bottom the sum of the two flux terms
 792 is an approximately linear function of H , as required for $\langle q'w' \rangle$ to be non-divergent over
 793 the boundary layer (section 3a). The scaling for the flux magnitude, $(1 + S_\infty^2)EBF_s$, is also
 794 shown (dashed black line). B) The same flux terms (as defined in the legend) decomposed by
 795 across-slope wavelength, where long wavelength motions ($\lambda_x > 100$ m, solid lines) are
 796 associated with the instability overturning cells, and small-scale motions ($\lambda_x < 100$ m, dashed
 797 lines) are associated with turbulence. The height of the low PV layer (H , large triangle) and
 798 the convective layer (h , small triangle) are indicated along the right ordinate in each plot. 51
- 799 **Fig. 10.** Comparison of the convective layer depth predicted from (33), h , and the depth determined
 800 from the numerical simulations, h_{NUM} . The squared correlation coefficient is shown in the
 801 plot title. For the numerical simulations the height of the convective layer is determined as
 802 the lowest height where $\overline{\langle w'b' \rangle}^T \leq 0$, where the overbar indicates averaging over 1 inertial
 803 period and turbulent motions are defined as having a cross-slope wavelength of $\lambda_x < 100$
 804 m. Instances where the bottom diffusive flux of perturbation buoyancy, κN_∞^2 , is of similar
 805 magnitude as the EBF_s are excluded for consistency with the assumptions of section 3 (see
 806 appendix). 52
- 807 **Fig. 11.** As in figure 3, but for run CONV-1 on day 12. In this simulation, where $L_s/H \gg 1$, SI/CI
 808 does not develop, and convective turbulence keeps the boundary layer unstratified. 53
- 809 **Fig. 12.** Cross-frontal section detailing the spatial distribution of the fastest growing instability type
 810 predicted from linear theory for run CONV-1 on day 12 (as in figure 11). See the caption of
 811 figure 4 for definitions. 54
- 812 **Fig. 13.** Comparison of the true lateral shear production (LSP) to the true vertical shear production
 813 (VSP), and total shear production (SP) for run CI-1 (left) and SI-1 (right). Profiles are
 814 averaged over days 4-6. In simulation CI-1, where $S_\infty > 1$, LSP exceeds VSP outside the
 815 convective layer, whereas VSP dominates the total shear production everywhere for simula-
 816 tion SI-1 ($S_\infty < 1$), consistent with the expectation from (41) and (42). The height of the low
 817 PV layer (H , large triangle) and the convective layer (h , small triangle) for each simulation
 818 are indicated along the right ordinates. 55
- 819 **Fig. 14.** Cumulative energy budget over the first 15 days of simulation SI-1, formed by taking the
 820 slope-normal integral of (35), and then integrating in time. 56
- 821 **Fig. 15.** Comparison between eddy kinetic energy production and dissipation. Panel a and b show
 822 slope-normal profiles of shear production (SP), vertical buoyancy production (VBP), and
 823 dissipation (DISS) from simulation CI-1 (panel a) and SI-1 (panel b), averaged over
 824 days 4-6. Terms are defined as in (35). Also shown is minus the EBF_s (gray dashed-dot line)
 825 and the scaling for the dissipation (black dashed line) given in equation (48). Panel c shows a
 826 comparison between the scaling for the depth-integrated dissipation rate and the geostrophic
 827 shear production plus the buoyancy production across all simulations. Note that here these
 828 terms are evaluated using the approximate form given by (47), ie.
 829 $GSP_s = -\langle v'w' \rangle N_\infty^2 \theta / f(1 + S_\infty^2)$ and $VBP = \langle w'b' \rangle / (1 + S_\infty^2)$. The simulation with
 830 $V_\infty = 0.2$ m s⁻¹ is off the scale shown on this plot, however it also closely follows the 1-1 line and is
 831 included in the squared correlation coefficient shown in the plot title. 57
- 832 **Fig. 16.** Evolution of the average along-slope bottom stress, $\langle \tau^y \rangle$, for all simulations (table 1). The
 833 top panel shows the evolution of the stress as a function of time. The bottom panel shows the
 834 stress evolution with time normalized by the Ekman adjustment timescale, which collapses

all simulations to a single curve (similar to the results for 1D simulations shown in Brink and Lentz 2010). Simulations with active SI/CI (circular markers) are normalized using the timescale (50), and simulations where convection dominates (diamond markers) are normalized using (51). In both plots the stress is averaged over 12 hour periods, and normalized by the maximum value for each simulation.

43



840 FIG. 1. Schematic of the numerical model domain (panel A), with initial condition consisting of a uniformly
 841 stratified interior (with buoyancy contours indicated by thin black lines) and barotropic interior flow over a
 842 sloping lower boundary. An example of the adjustment of the boundary layer towards thermal wind balance
 843 is shown in panel B, where downslope Ekman transport generates thermal wind shear in the bottom boundary
 844 layer, reducing the near-bottom velocities. The rotated coordinate system is also shown, with standard non-
 845 rotated coordinates denoted using the hat notation.



846 FIG. 2. Overview of the evolution of simulation SI-1 (with parameters as given in table 1). From top to bottom
 847 the panels give the across-slope velocity (u), the total along-slope velocity ($v_T = v + V_\infty$), the vertical buoyancy
 848 gradient (N^2), and the PV (q). All values are averaged in the across-slope (x) direction, and normalized as
 849 indicated in each plot. The evolution of the low PV layer depth H , as predicted by (27), is shown in the bottom
 850 panel in black.

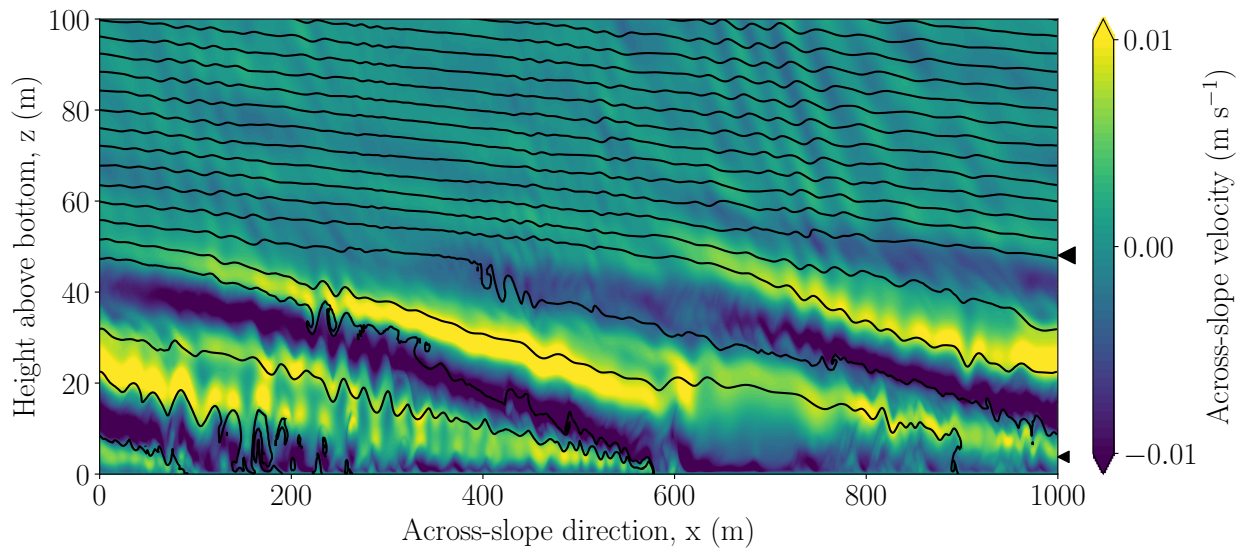
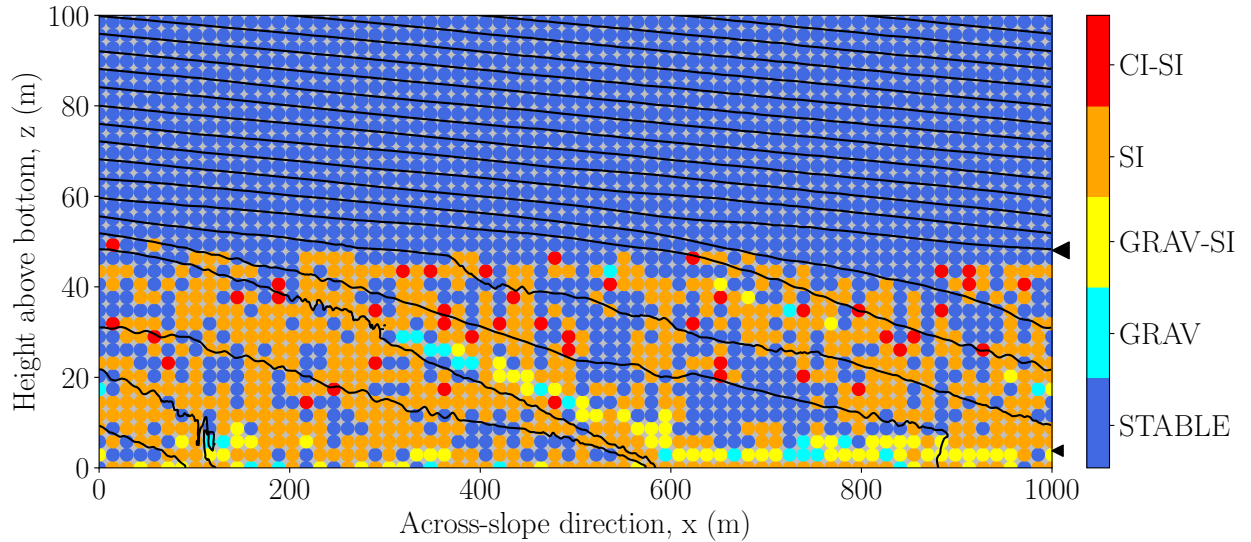


FIG. 3. Snapshot of the across-slope velocity field (u , color scale) from day 12 of run SI-1. The banded velocity structure is typical of symmetric instability, where the fastest growing mode is oriented along isopycnals (black contours). The height of the low PV layer (H , section 3b) and the convective layer (h , section 3c) as determined from the numerical solutions are indicated along the right ordinate by the large and small triangles, respectively.



856 FIG. 4. Cross-frontal section detailing the spatial distribution of the fastest growing instability type predicted
 857 from linear theory for run SI-1 on day 12 (as in figure 3). Parameter space is divided into mixed centrifugal-
 858 symmetric (CI-SI), symmetric (SI), gravitational (GRAV), and mixed gravitational-symmetric (GRAV-SI) fol-
 859 lowing the balanced Richardson number criteria laid out in Thomas et al. (2013, as discussed in section 2b).
 860 Isopycnals are shown with black contours. All fields are averaged over a 4 hour period, and the height of the low
 861 PV layer (H , section 3b) and the convective layer (h , section 3c) as determined from the numerical solutions are
 862 indicated along the right ordinate by the large and small triangles, respectively.

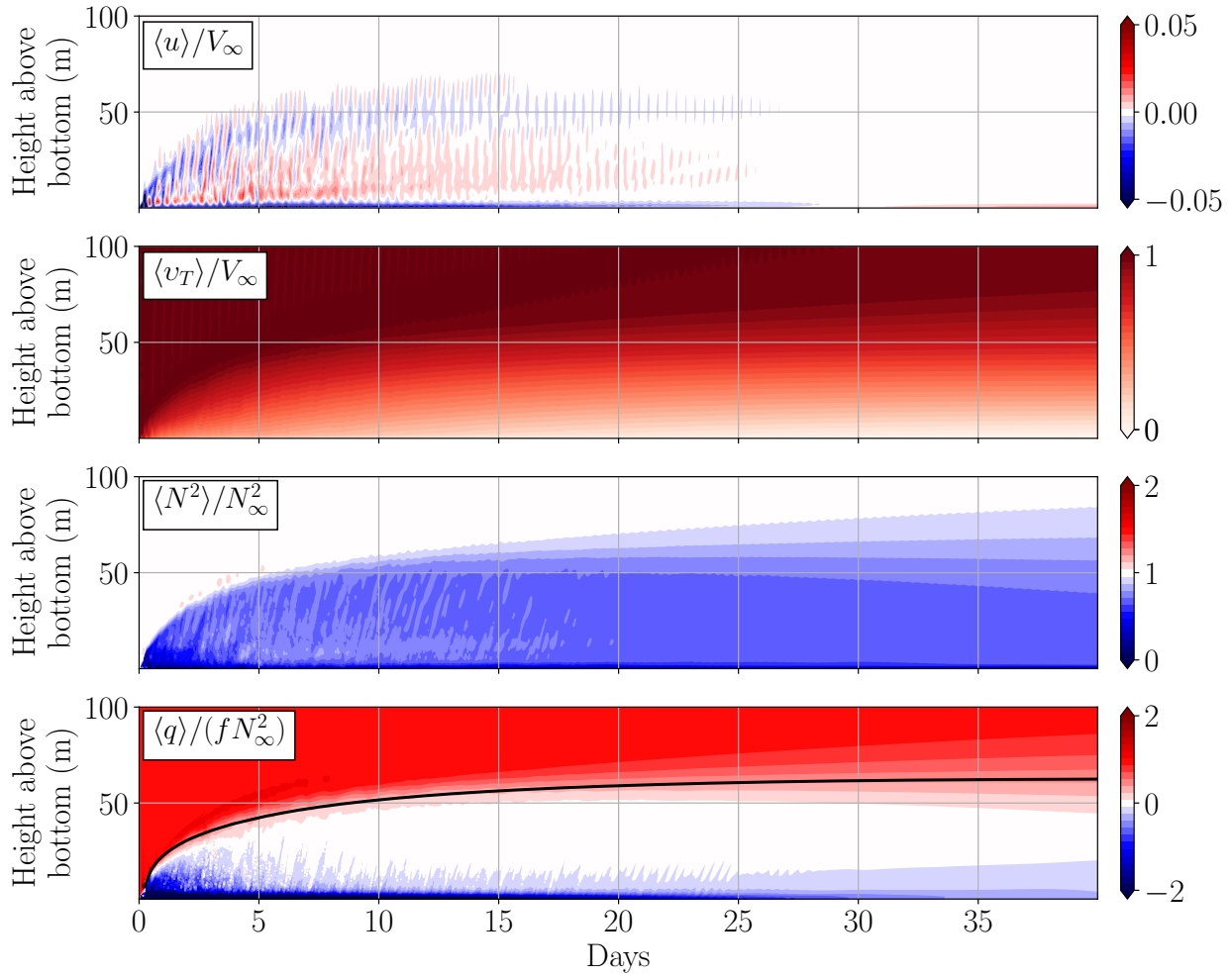


FIG. 5. As in figure 2, but for simulation CI-1 (with parameters as given in table 1). From top to bottom the panels give the across-slope velocity (u , note the reduced color scale from figure 2), the total along-slope velocity ($v_T = v + V_\infty$), the vertical buoyancy gradient (N^2), and the PV (q). All values are averaged in the across-slope (x) direction, and normalized as indicated in each plot. The evolution of the low PV layer depth H , as predicted by (27), is shown in the bottom panel in black.

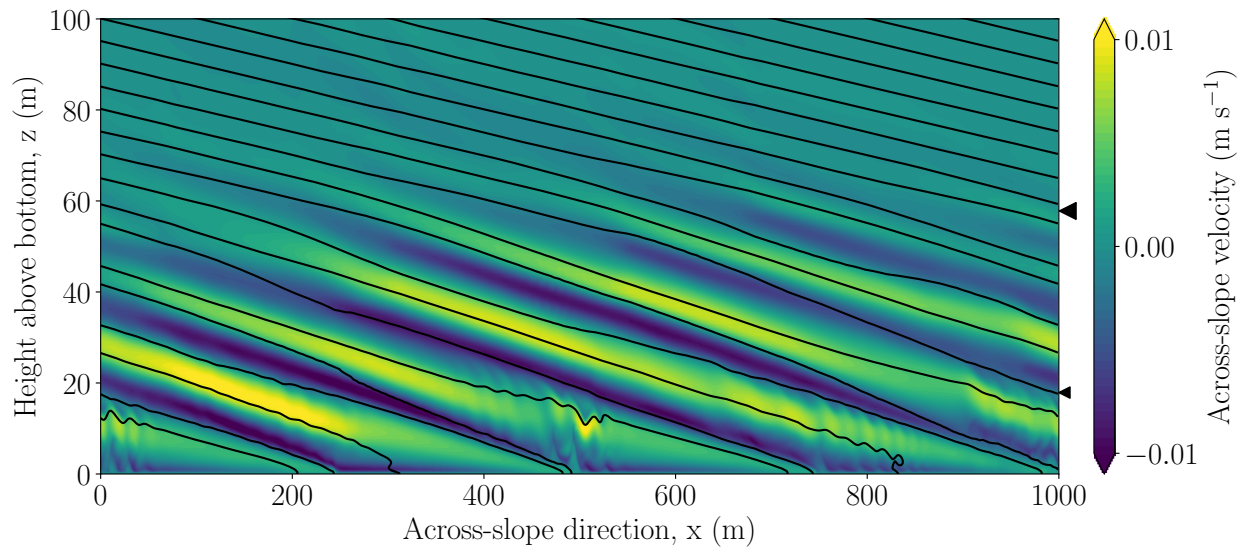
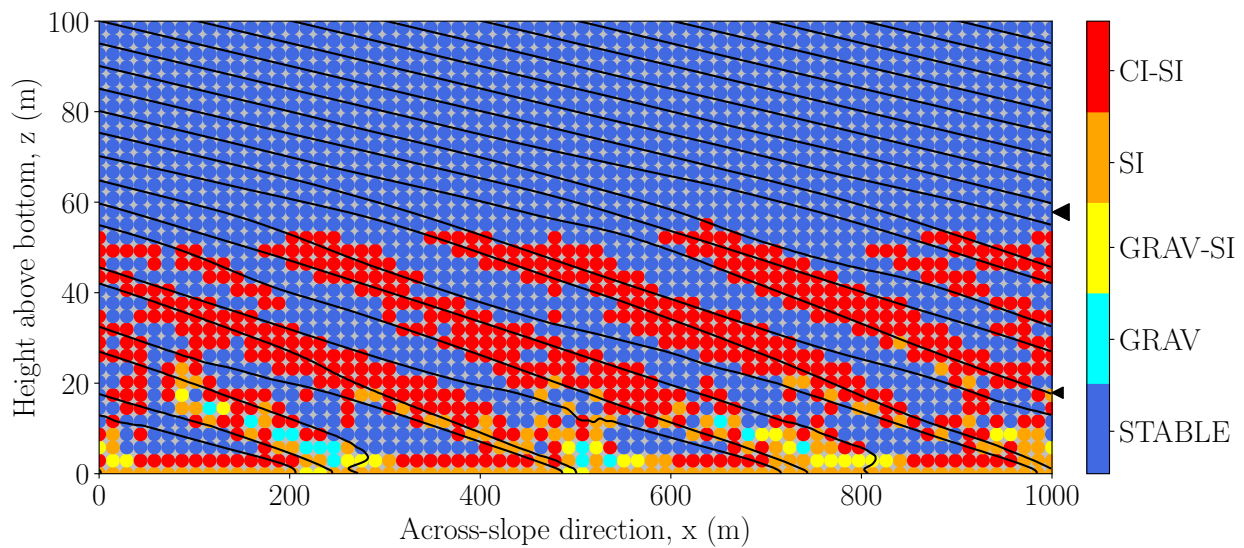


FIG. 6. As in figure 3, but for run CI-1 on day 12.



868 FIG. 7. Cross-frontal section detailing the spatial distribution of the fastest growing instability type predicted
 869 from linear theory for run CI-1 on day 12 (as in figure 6). See the caption of figure 4 for definitions.

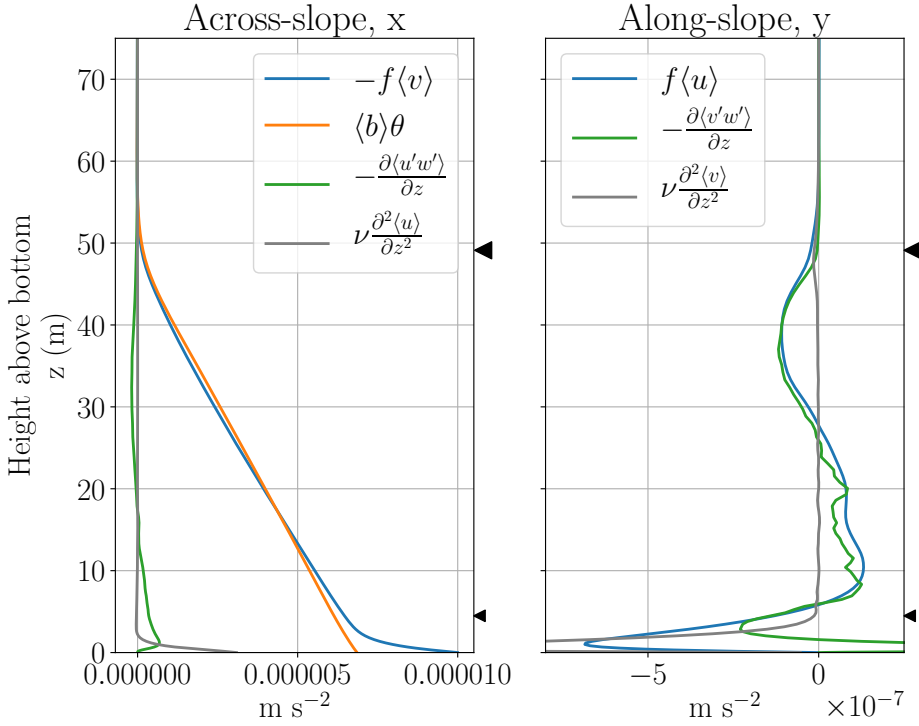


FIG. 8. Dominant terms in the momentum equations for simulation SI-1, averaged in the across-slope direction (x) and over days 11-13. The across-slope momentum budget, (7), is largely in a geostrophic balance between buoyancy perturbations and Coriolis accelerations, with some additional contribution from the turbulent momentum flux divergence (left panel). The along-slope momentum budget, (8), is in approximate Ekman balance, with Coriolis accelerations balancing the turbulent momentum flux divergence (right panel). The height of the low PV layer (H , large triangle) and the convective layer (h , small triangle) are indicated along the right ordinate in each plot.

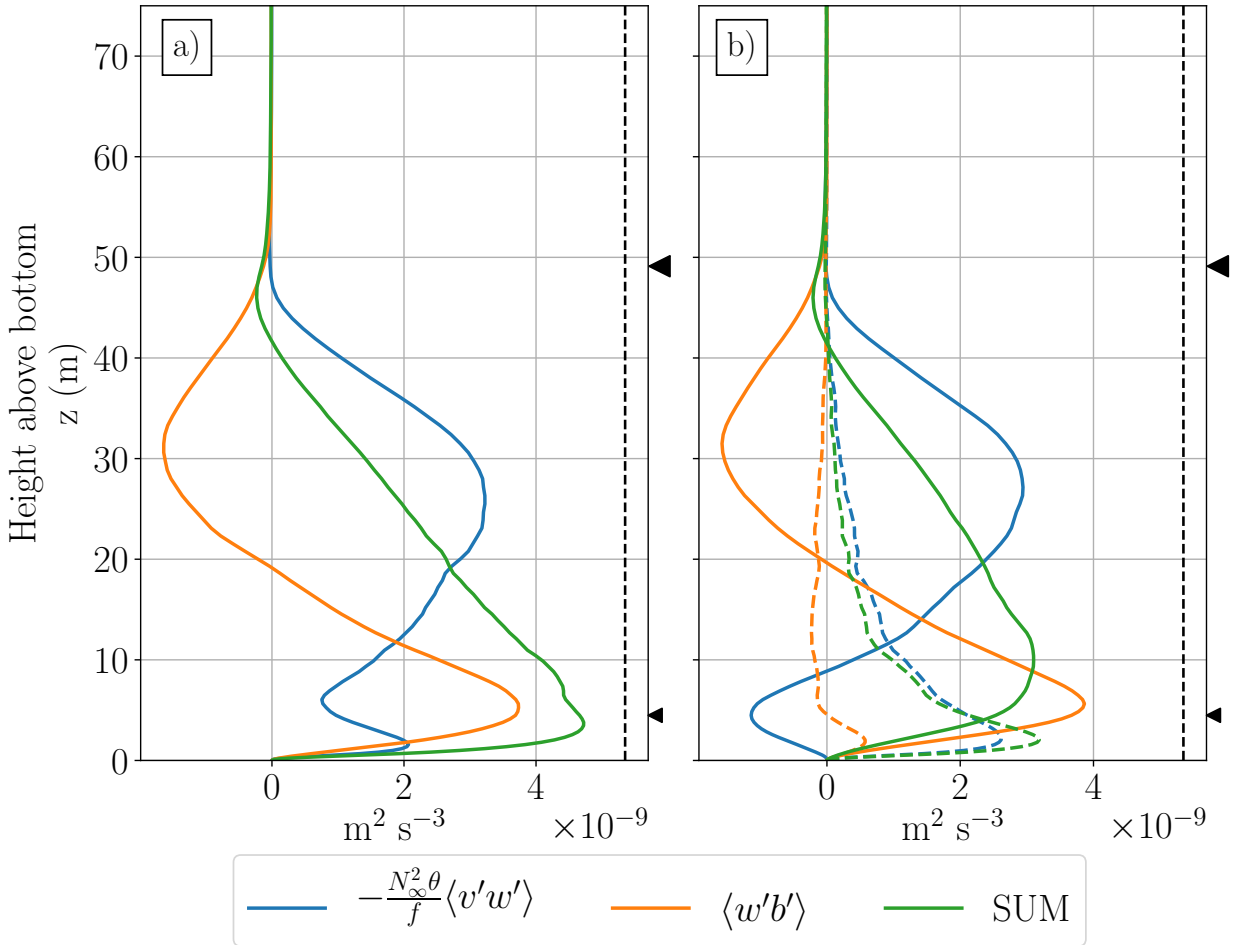
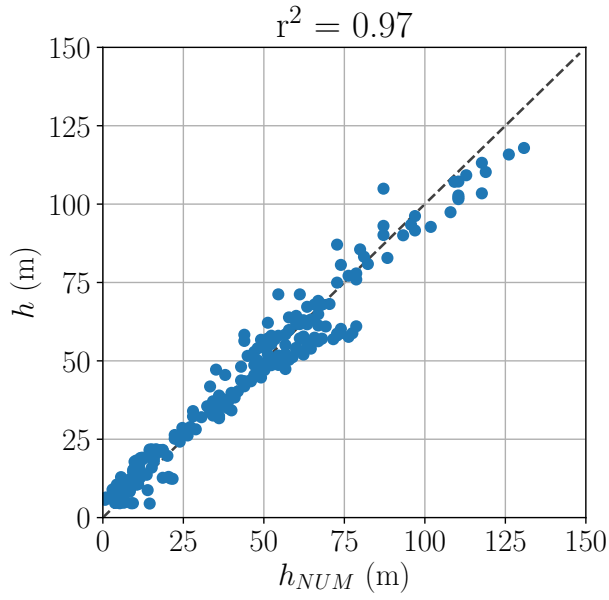
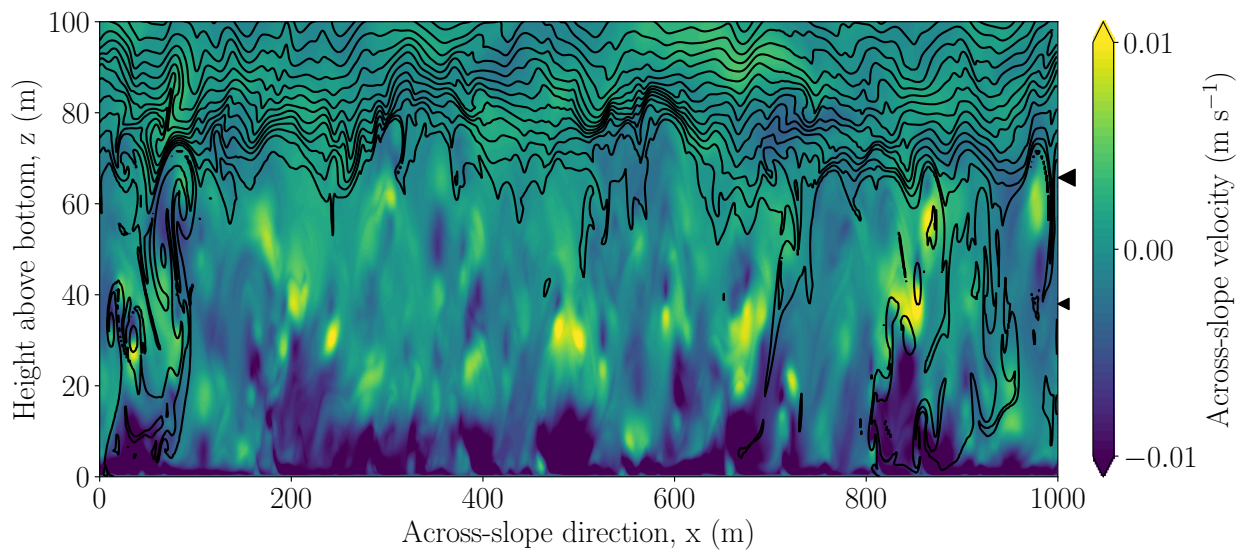


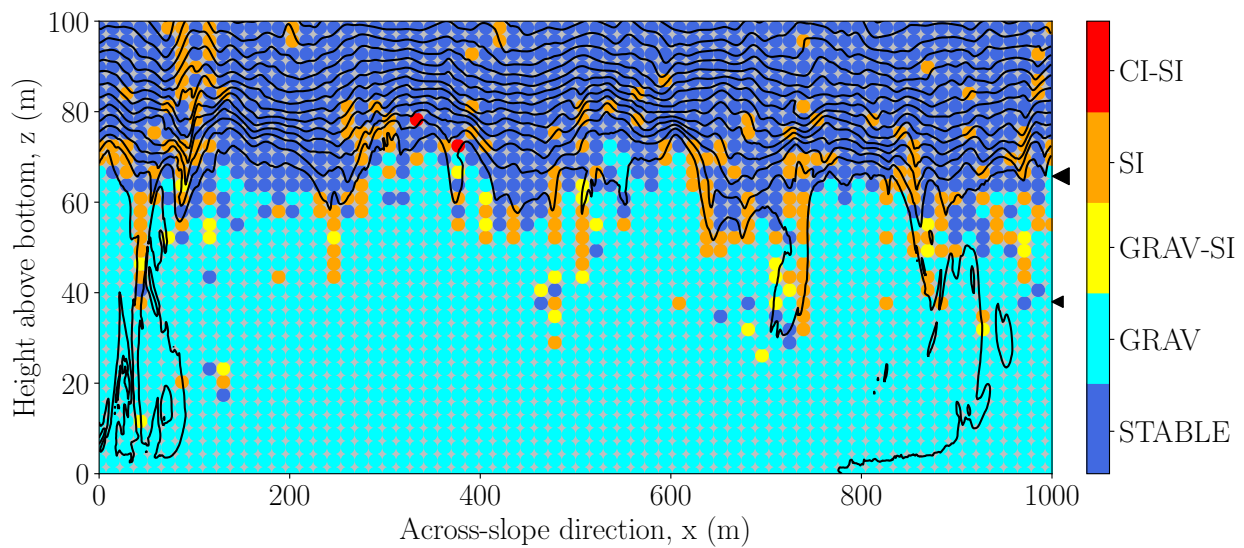
FIG. 9. Terms from the slope-normal PV flux equation, (19), averaged horizontally (x) and over days 11–13 for simulation SI-1. A) Away from the bottom the sum of the two flux terms is an approximately linear function of H , as required for $\langle q' w' \rangle$ to be non-divergent over the boundary layer (section 3a). The scaling for the flux magnitude, $(1 + S_\infty^2)EBF_s$, is also shown (dashed black line). B) The same flux terms (as defined in the legend) decomposed by across-slope wavelength, where long wavelength motions ($\lambda_x > 100 \text{ m}$, solid lines) are associated with the instability overturning cells, and small-scale motions ($\lambda_x < 100 \text{ m}$, dashed lines) are associated with turbulence. The height of the low PV layer (H , large triangle) and the convective layer (h , small triangle) are indicated along the right ordinate in each plot.



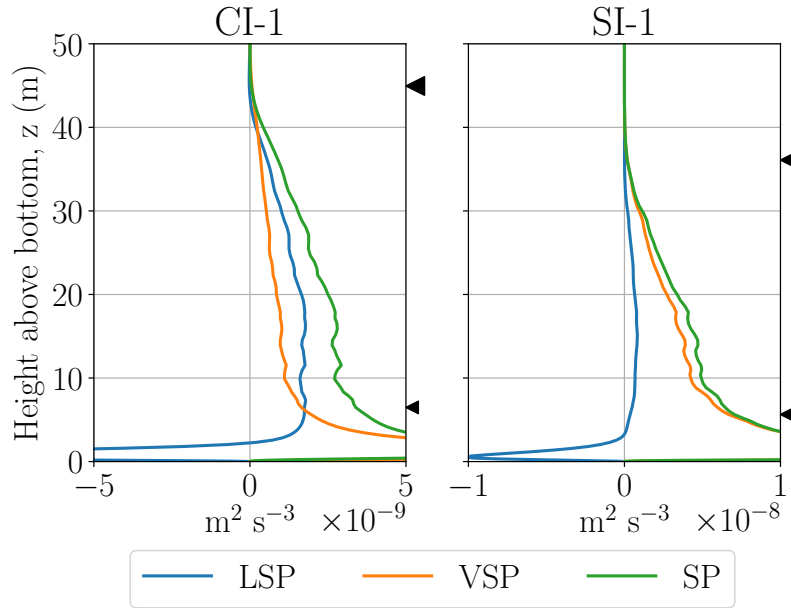
885 FIG. 10. Comparison of the convective layer depth predicted from (33), h , and the depth determined from the
 886 numerical simulations, h_{NUM} . The squared correlation coefficient is shown in the plot title. For the numerical
 887 simulations the height of the convective layer is determined as the lowest height where $\overline{\langle w'b' \rangle}^T \leq 0$, where the
 888 overbar indicates averaging over 1 inertial period and turbulent motions are defined as having a cross-slope
 889 wavelength of $\lambda_x < 100$ m. Instances where the bottom diffusive flux of perturbation buoyancy, κN_∞^2 , is of
 890 similar magnitude as the EBF_s are excluded for consistency with the assumptions of section 3 (see appendix).



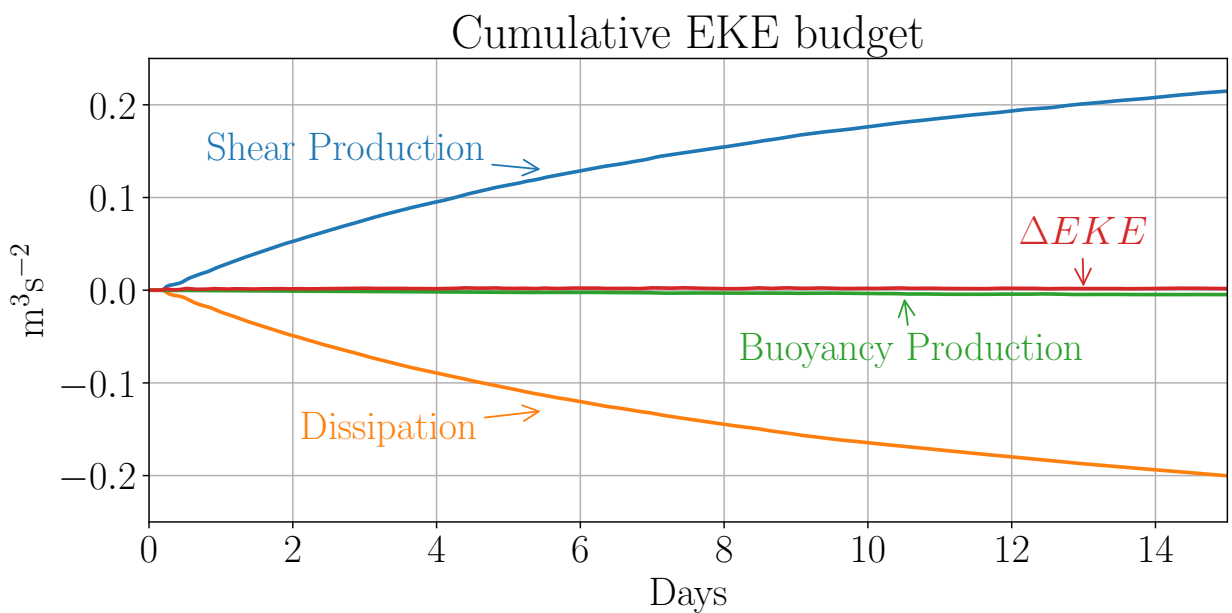
891 FIG. 11. As in figure 3, but for run CONV-1 on day 12. In this simulation, where $L_s/H \gg 1$, SI/CI does not
 892 develop, and convective turbulence keeps the boundary layer unstratified.



893 FIG. 12. Cross-frontal section detailing the spatial distribution of the fastest growing instability type predicted
 894 from linear theory for run CONV-1 on day 12 (as in figure 11). See the caption of figure 4 for definitions.



895 FIG. 13. Comparison of the true lateral shear production (LSP) to the true vertical shear production (VSP),
 896 and total shear production (SP) for run CI-1 (left) and SI-1 (right). Profiles are averaged over days 4-6. In
 897 simulation CI-1, where $S_\infty > 1$, LSP exceeds VSP outside the convective layer, whereas VSP dominates the total
 898 shear production everywhere for simulation SI-1 ($S_\infty < 1$), consistent with the expectation from (41) and (42).
 899 The height of the low PV layer (H , large triangle) and the convective layer (h , small triangle) for each simulation
 900 are indicated along the right ordinates.



901 FIG. 14. Cumulative energy budget over the first 15 days of simulation SI-1, formed by taking the slope-
 902 normal integral of (35), and then integrating in time.

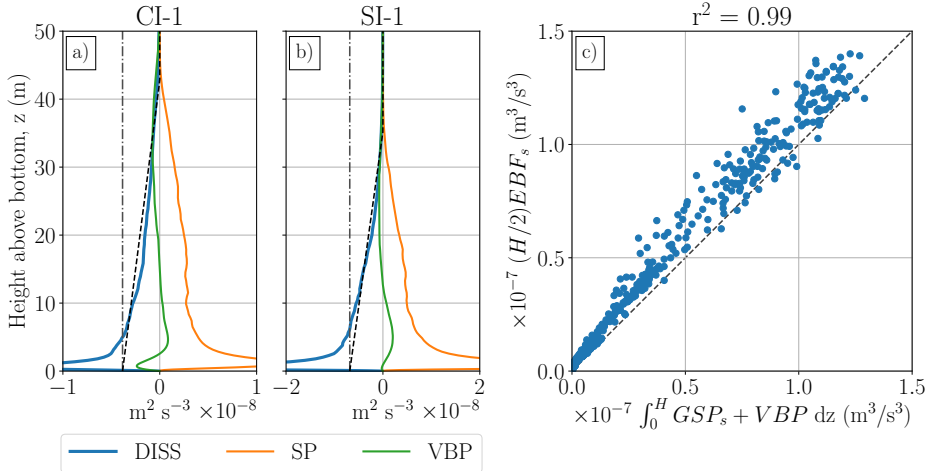
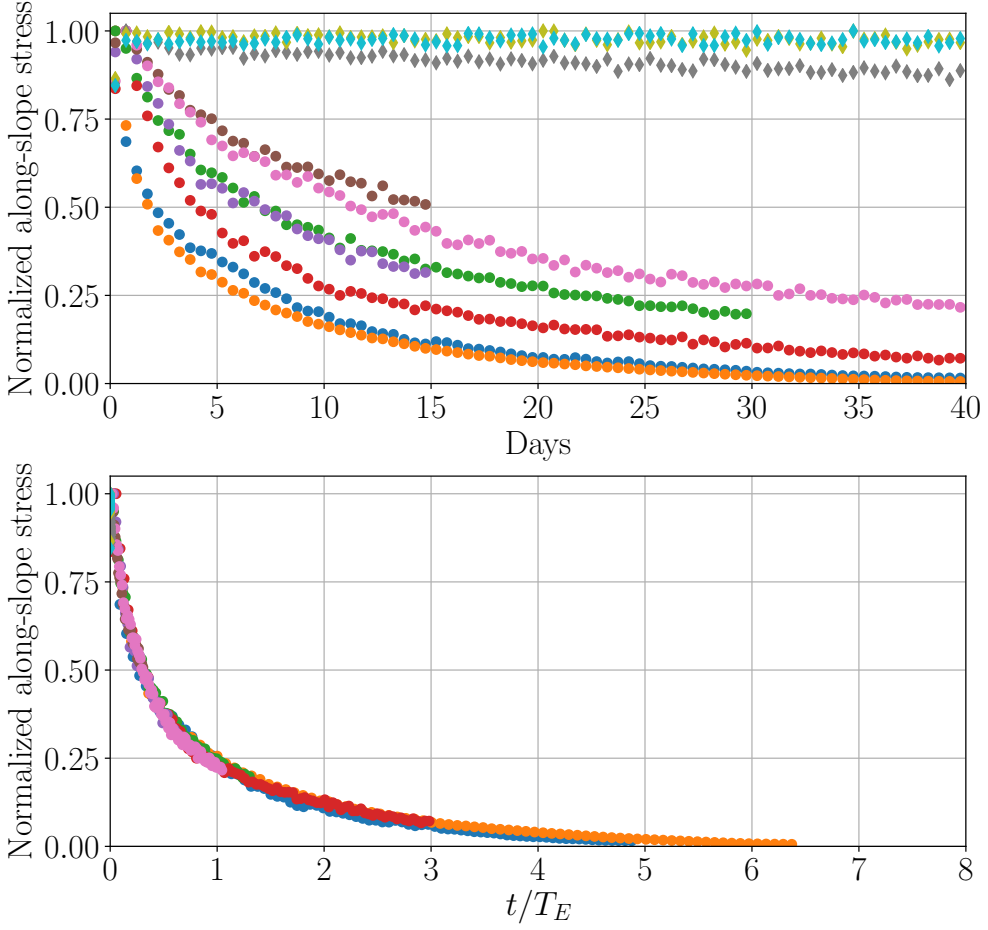


FIG. 15. Comparison between eddy kinetic energy production and dissipation. Panel a and b show slope-normal profiles of shear production (SP), vertical buoyancy production (VBP), and dissipation (DISS) from simulation CI-1 (panel a) and SI-1 (panel b), averaged over days 4-6. Terms are defined as in (35). Also shown is minus the EBF_s (gray dashed-dot line), and the scaling for the dissipation (black dashed line) given in equation (48). Panel c shows a comparison between the scaling for the depth-integrated dissipation rate and the geostrophic shear production plus the buoyancy production across all simulations. Note that here these terms are evaluated using the approximate form given by (47), ie. $GSP_s = -\langle v'w' \rangle N_\infty^2 \theta / f(1 + S_\infty^2)$ and $VBP = \langle w'b' \rangle / (1 + S_\infty^2)$. The simulation with $V_\infty = 0.2 \text{ m s}^{-1}$ is off the scale shown on this plot, however it also closely follows the 1-1 line and is included in the squared correlation coefficient shown in the plot title.



912 FIG. 16. Evolution of the average along-slope bottom stress, $\langle \tau^y \rangle$, for all simulations (table 1). The top panel
913 shows the evolution of the stress as a function of time. The bottom panel shows the stress evolution with time
914 normalized by the Ekman adjustment timescale, which collapses all simulations to a single curve (similar to the
915 results for 1D simulations shown in Brink and Lentz 2010). Simulations with active SI/CI (circular markers)
916 are normalized using the timescale (50), and simulations where convection dominates (diamond markers) are
917 normalized using (51). In both plots the stress is averaged over 12 hour periods, and normalized by the maximum
918 value for each simulation.